Ore Geology Reviews 119 (2020) 103316

Contents lists available at ScienceDirect

Ore Geology Reviews

journal homepage: www.elsevier.com/locate/oregeorev

# The evolution of the Dominga Fe-Cu deposit (northern Chile): Insights from mineral textures and micro-CT analysis

Gert Heuser[a,b,*,1], Gloria Arancibia[a,b,c,d,2], Eugenio E. Veloso[a,c,3], José Cembrano[a,c,4], Pedro Filipe Oliveira Cordeiro[b,e,5], Mathias Nehler[f,6], Rolf Bracke[f,7]

[a] Departamento de Ingeniería Estructural y Geotécnica, Pontificia Universidad Católica de Chile, Santiago, Chile
[b] Millenium Nucleus for Metal Tracing Along Subduction, Universidad de Chile, FCFM, Santiago, Chile
[c] Andean Geothermal Center of Excellence (CEGA), FCFM, Universidad de Chile, Santiago, Chile
[d] Centro de Investigación en Nanotecnología y Materiales Avanzados (CIEN-UC), Pontificia Universidad Católica de Chile, Santiago, Chile
[e] Departamento de Ingeniería de Minería, Pontificia Universidad Católica de Chile, Santiago, Chile
[f] International Geothermal Centre (GZB), Bochum, Germany

ARTICLE INFO

*Keywords:*
Fluid flow mechanisms
Fault zone
Mineral texture
Fluid flow simulation
Northern Chile
Ore deposit

ABSTRACT

The Fe-Cu Dominga deposit (2082 Mt at 23% Fe, 0.07% Cu), located in the Coastal Cordillera of northern Chile, is hosted by volcanic rocks of the Punta del Cobre Formation (131.5 ± 1.5 Ma zircon U-Pb) and into sub-volcanic units (Dioritic Complex, 131.6 ± 1.0 Ma zircon U-Pb). The Fe-Cu mineralization is controlled by three structural systems which developed from a transtensional to a transpressional tectonic regime and can be divided into three groups: Early iron, Late iron and Early copper ores. Early iron ores are comprised of magnetite + pyrite + biotite breccia (1A ore), veins (1B ores), layers (1C ores) and disseminated ores (1D ores). Late iron ores are characterized by two groups of magnetite-apatite-actinolite hydrothermal breccias (2A, 2C ores) and syntaxial/antitaxial veins (2B, 2D, 2E ores). Early copper ores occur as syntaxial K-feldspar and quartz + epidote + chalcopyrite veins (3A ores), and as anhydrite + chalcopyrite-rich matrix breccia and veins (3B ores). This work presents a detailed mineral texture study of veins, hydrothermal breccias and disseminated iron-rich layers of the Dominga deposit which aims to determine fluid flow mechanisms associated with both iron and copper ores. The description of vein and breccia textural and internal structures was conducted in thin/polished sections perpendicular and parallel to the wall using optical and Scanning Electron Microscope techniques. In addition, two oriented surface samples were analyzed by computerized X-ray microtomography and numerical fluid flow simulations through the Lattice-Boltzmann method to obtain (3D) permeability anisotropy associated with early iron ores. Microtextures associated with Dominga iron and copper ores suggest that the main mass transfer fluid flow mechanism corresponds to advection (channelized and pervasive fluid flow), regardless of the tectonic regime. However, early copper ores have more complex mineral textures and internal structure due to the recurrence of crack-seal episodes. We propose that the various mineral textures and structures indicate changes in fluid flow direction over time, controlled by the permeability anisotropy of each tectonic regime. Results from numerical fluid flow simulations of early iron ore (1B) veins show a higher value of structural permeability in the vertical direction ($k_{Vz}$), which is consistent with a transtensional tectonic regime and the formation of vertical veins. Moreover, permeability related to 1C layered ore is higher in horizontal directions ($k_{Hx}$, $k_{Hy}$) rather than vertical ($k_{Vz}$) because of the natural permeability anisotropy of volcaniclastic rocks parallel to bedding. However, the $k_{Vz}$ value suggests that the development of such layered ores also exhibits a degree of structural control at several length scales consistent with a transtensional regime. These results indicate that the occurrence of early iron ores as veins and layers may be controlled by both primary

* Corresponding author at: Departamento de Ingeniería Estructural y Geotécnica, Pontificia Universidad Católica de Chile, Santiago, Chile.
*E-mail address:* gkheuser@uc.cl (G. Heuser).
[1] ORCID: 0000-0001-5473-7356.
[2] ORCID: 0000-0003-2860-1302.
[3] ORCID: 55901391600.
[4] ORCID: 6602813874.
[5] ORCID: 0000-0003-1996-9551.
[6] ORCID: 57207550681.
[7] ORCID: 24315671000.

https://doi.org/10.1016/j.oregeorev.2020.103316
Received 24 June 2019; Received in revised form 23 November 2019; Accepted 4 January 2020
Available online 11 January 2020

permeability anisotropy related to each lithology present at the Dominga Fe-Cu deposit and to the tectonic regime at the time. Finally, the Dominga Fe-Cu deposit attests to long lived hydrothermal activity with a transition from early fluids capable of precipitating iron ores under a transtensional system to later-stage fluids which precipitated copper ores under a transpressional regime that generated multiple crack and seal episodes.

## 1. Introduction

Faults zones are discontinuities within the Earth's crust developed as a kinematic response to the stress field imposed on the rock mass (e.g. Fossen and Tikoff, 1998). Faults occur at different scales, from thousands of kilometers down to millimetric fractures, keeping geometric properties such as width and length invariant over several orders of magnitude (Faulkner et al., 2011; Jensen et al., 2011). Fault zones play an important role in the genesis of ore deposits because they can modify rock permeability by either allowing the emplacement and storage of hydrothermal fluids or by sealing conduits and hindering mineralization processes (e.g. Tosdal and Richards, 2001; Micklethwaite et al., 2010). Therefore, the interaction of fault zones and fluids in the upper crust is a topic of fundamental interest to understand and predict sites where ore deposits might have emplaced.

The relationship between the orientation and magnitude of the principal stress axes ($\sigma_1$, $\sigma_2$, $\sigma_3$), tectonic setting and permeability determines spatial orientation, distribution of fractures patterns and favorable directions for fluid flow. Fractures likely develop maximum permeability anisotropy following $\sigma_2$ and parallel to $\sigma_1$ (Sibson, 1994;

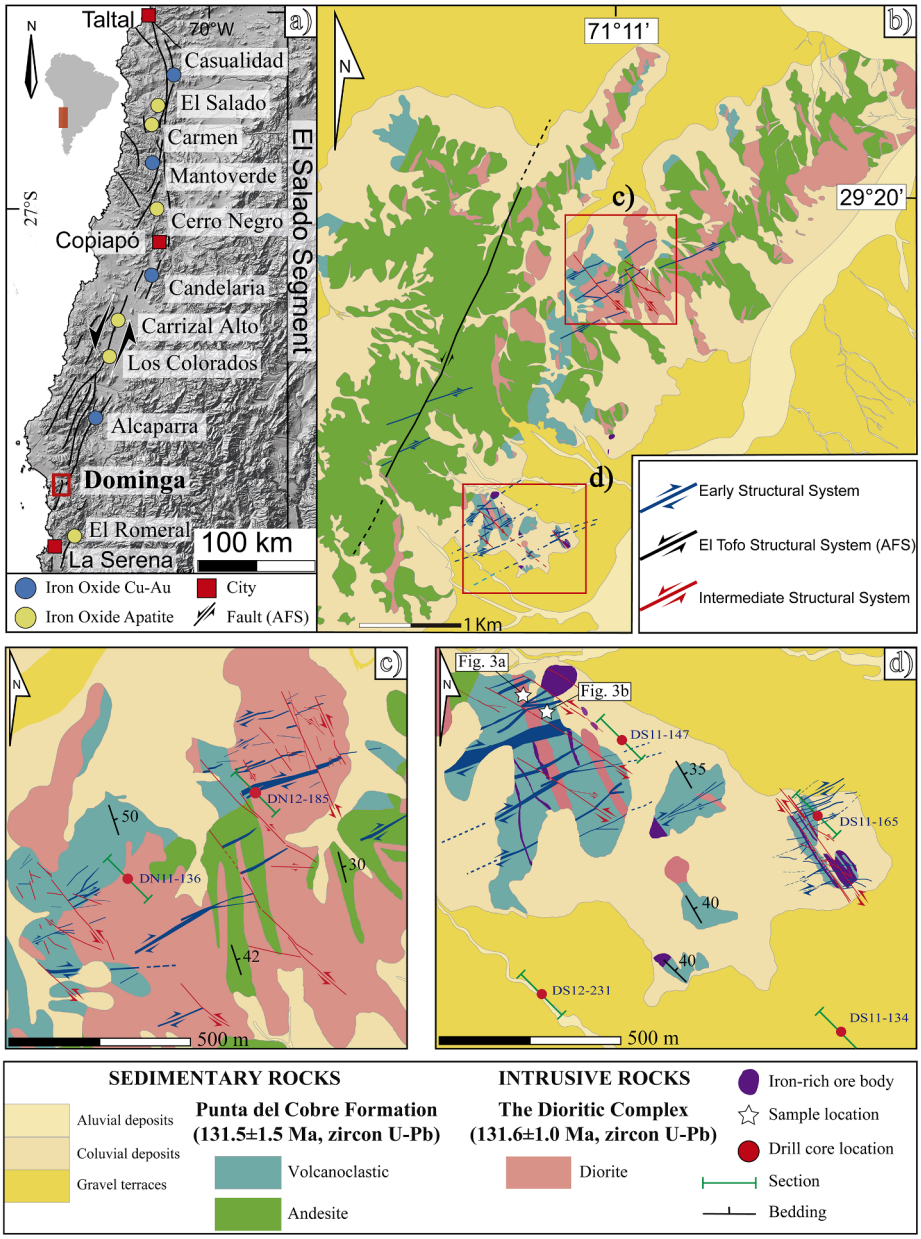


**Fig. 1.** Location and geology of the Dominga Fe-Cu deposit. a Tectonic setting and spatial distribution of some IOA and IOCG ore deposits within the CIB at the El Salado segment of the Atacama Fault System. b Simplified geologic and structural map of the Dominga Fe-Cu deposit. C–d Simplified geologic and structural map of north and south Dominga, respectively. Drill-hole locations and structural sections are indicated. Radiometric ages from Creixell and Arévalo (2009).

Cox, 2005; Rowland and Simmons, 2012; Faulkner and Armitage, 2013). Thus, within a fault zone, fluids circulate both through the interconnected network of fractures (secondary permeability) often known as the damage zone (Faulkner et al., 2008, 2010) and in the host rock, through connected pore spaces (primary permeability).

However, the capacity of a fluid to flow within a natural system (e.g. ore deposit, geothermal reservoir) changes over time because plate motion and tectonic regimes are dynamic (e.g. Young et al., 2018). Seismic activity, for example, can lead to instantaneous changes in differential stress and abrupt variation of fluid pressure and/or direction, possibly changing permeability, and consequently fluid migration and mineral precipitation (Sibson, 2004). The mineral precipitation necessary to generate ore deposits decreases rock permeability. Hence, multiple episodes of fracturing and deformation are required to maintain and/or enhance the permeability of rocks in order to channel and store high volumes of fluid required to form a hydrothermal deposit (e.g. Faulkner et al., 2010; Gudmundsson et al., 2010). Consequently, the permeability conditions of a single fault zone can vary over time and allow for multiple ore geometries such as veins, hydrothermal breccias, and intergranular disseminated mineralization. Here, the internal structure and mineral textures in terms of shape, size and orientation of crystals within veins and hydrothermal breccia can record information about fault propagation and growth (e.g. Kim et al., 2004). For example, these characteristics have been studied in order to understand how fluid flow mechanisms related to fault zone activity (e.g. fault-valve mechanism, crack-seal; Sibson, 1994; Ramsay, 1980), mass transfer (e.g. advection, diffusion; Oliver and Bons, 2001; Hilgers et al., 2004), kinematics during mineral precipitation (e.g. Power and Tullis, 1989; Uysal et al., 2011), strain rate (Hilgers et al., 2001) and fluid properties (e.g. T°, P°, Mitchell et al., 2017).

An example of the interaction between tectonic setting, the development of fault zones and the transport and emplacement of Fe-Cu-Au-rich fluids has been observed in ore deposits of the Coastal Range of northern Chile, all of which exhibit evidence of structural control (e.g. Bonson et al., 1996; Grocott and Taylor, 2002; Cembrano et al., 2009). Some of the best documented cases of structural control in ore deposits genesis associated with a dynamic tectonic regime are located in northern Chile, along the Atacama Fault System (AFS, Ruiz et al., 1965). The AFS has been spatially and genetically related to the migration of Fe-Cu-Au bearing-fluids responsible for several Iron Oxide Apatite (IOA) and Iron Oxide Copper-Gold (IOGC) deposits of the Coastal Cordillera of northern Chile (e.g. Bonson et al., 1996; Vila et al., 1996; Sillitoe, 2003; Arévalo et al., 2006; Rieger et al., 2010).

A remarkable example of the importance of spatial and genetic affinity between fault zones and Fe-Cu mineralization within the AFS can be observed in the Dominga Fe-Cu deposit (2082 Mt at 23.3% Fe and 0.07% Cu). In Dominga, an early transtensional regime developed fault zones within which Fe-rich mineralizing-fluids emplaced, and a later transpressional regime allowed for the circulation of a Cu-bearing-fluid (Veloso et al., 2017). Accordingly, this deposit constitutes a superb case study to explore the nature of the relationship between ore mineral deposition and variations in tectonic regimes and fluid flow. However, the spatial and temporal evolution of this important fault system and consequent changes in stress vectors leading to ore mineral precipitation remains underexplored.

To address these issues, this work presents a detailed microstructure and mineral texture analyses of veins, hydrothermal breccias and disseminated Fe-rich layers of the Dominga deposit. Also, using the Lattice-Boltzmann method, we measured the permeability anisotropy related to magnetite veins in two representative types of rock found in the Dominga deposit (volcaniclastic and diorite rocks) as well as the permeability anisotropy related to disseminated Fe-rich layers in volcaniclastic rocks (primary permeability). Data were used to unravel how different mineral textures formed under their corresponding tectonic regimes.

## 2. Geological setting

The Dominga iron deposit is located at the southern tip of the Cretaceous Chilean Iron Belt (CIB), a North-South belt located roughly between 26° and 30° S in the Coastal Cordillera of northern Chile (Fig. 1a). Ore deposits within the CIB (e.g. Mantoverde, Candelaria, Los Colorados) developed in an active plate margin during the Early-Middle Jurassic to Middle Cretaceous as a consequence of sinistral oblique subduction of the Aluk Plate beneath the South American Plate, along the western margin of Gondwana (Coira et al., 1982). This period was characterized by abundant volcanism and plutonism (Scheuber and Gonzales, 1999; Parada et al., 2007) and marked by the genesis of several ore deposits in the CIB. According to Chen et al. (2013), the initial phase of IOCG mineralization developed during the Middle Jurassic (165–155 Ma), whereas the peak of IOCG-IOA formation occurred during the mid-Cretaceous ca. 130–100 Ma (Oyarzún et al., 2003). The interaction between magmatism and strain partitioning in this intra-arc fault system was followed by arc abandonment, cooling and the development of brittle fault systems (e.g. Wilson and Grocott, 1999; Grocott and Taylor, 2002).

Various works have suggested that the main fault system responsible for controlling the emplacement of ore deposits of the CIB is the AFS (e.g., Geijer, 1931; Ruiz et al., 1965; Park, 1972; Oyarzún and Frutos, 1984; Espinoza, 1984 1990; Ruiz and Peebles, 1988; Sillitoe, 2003: Rieger et al., 2010). The Atacama Fault is a ~1000 km long, margin-parallel, strike-slip fault system (Fig. 1a), with mostly NNE and NNW-striking steeply dipping fault branches of ductile shear zones reworked by left-lateral brittle faults (Brown et al., 1993). From north to south, the AFS has been subdivided into three segments of brittle and ductile faults: the Salar del Carmen, Paposo and El Salado segments (Naranjo, 1987; Thiele and Pincheira, 1987). The absolute age of ductile coeval left-lateral and dip-slip normal deformation of the El Salado Segment occurred at ca. 132 Ma; and sinistral displacement at ca. 130–116 Ma (Grocott and Taylor, 2002; Mathur et al., 2002). However, in some IOA deposits, mineralization was associated with a NE-ENE-striking dextral strike-slip fault systems). Geochonologic data (U-Pb in apatite-magnetite) from deposits such as Cerro Negro, El Salado, Carrizal Alto and Carmen suggest formation ages for the mineralization prior to the development of the AFS (ca. 130 Ma Gelcich et al., 2005; Ruiz et al., 1965; Bonson et al., 1996; Vivallo et al., 2008).

Among the deposits that are spatially associated with the Atacama Fault System, the Cretaceous Dominga Fe-Cu deposit exhibits evidence of both a NE-ENE-striking dextral strike-slip fault system that controls the emplacement of Fe-mineralization and a later sinistral fault system (El Tofo Fault) parallel to the AFS, controlling the Fe ≪ Cu-mineralization (Veloso et al., 2017).

## 3. Geology of the deposit

The Dominga Fe-Cu deposit is emplaced into volcanic and volcaniclastic rocks of the Punta del Cobre Formation (Creixell and Arévalo, 2009) and into diorites belonging to the so-called Dioritic Complex (Fig. 1b). The deposit can be divided geographically and in terms of dominant lithologies into North Dominga, mostly composed of diorite, and South Dominga, dominated by andesite and volcaniclastic rocks. In both areas, Fe-Cu mineralization was controlled by fault zones (Veloso et al., 2017). Three structural systems controlling the emplacement of alteration-mineralization stages can be defined by their cross-cutting relationships, preferential orientations, geometry, kinematics, and infill material. From oldest to youngest these are: 1) the Early Structural System, related to the Early and Late Fe mineralization Stage; 2) the El Tofo Structural System (parallel to the AFS), related to the Early Cu mineralization Stage; and 3) the Intermediate Structural System, related to the Late Cu mineralization Stage.

The Early Structural System corresponds to a N50°-70°E and -N80°-100°E-striking right-lateral strike slip duplex (Veloso et al., 2017). Fault

cores are ca. 1–25 m thick and composed of foliated (ultra)cataclasite with S-C fabrics and fault breccia. The Early Structural System is associated with the formation of disseminated biotite + quartz + magnetite( ± ) pyrite mineralization as stratiform bodies of the early Fe stage (Fig. 2). Veins and hydrothermal breccias of the late Fe stage associated with this system have variations in their infill mineral assemblages, with veins containing actinolite + magnetite whereas hydrothermal breccia are cemented by magnetite + apatite + actinolite + pyrite (U-Pb in apatite, 127.0 ± 15.0 Ma, Veloso et al., 2017).

The El Tofo Structural System is a N20°-40°E-striking left-lateral strike slip fault zone (Veloso et al., 2017) which corresponds to one of the southernmost faults strands of the AFS. It is characterized by a 2–20 m thick fault core associated with fault breccias and cataclasites. Veins and hydrothermal breccia related to the El Tofo Structural System show mineral assemblages such as quartz + k-feldspar + epidote + albite, and quartz + chalcopyrite + molybdenite + epidote + anhydrite early Cu stage (Re-Os in molybdenite 127.0 ± 0.6 Ma, Veloso et al., 2017). The Intermediate Structural System consists of a N30°-50°W-striking left-lateral strike slip duplex (Veloso et al., 2017) that offsets both previous systems. It is composed of fault breccia (ca. 1 m thick), veins and fault-veins with infills of calcite + quartz, calcite + hematite (specular), and calcite ± chalcopyrite ± Cu oxide that characterize the late Cu stage.

Based on best-fit stress field analysis, Veloso et al, (2017) concluded that structural systems in the Dominga deposit represent the progression of tectonic regimes. The Early Structural System is compatible with a transtensional solution with subhorizontal $\sigma_1$ and $\sigma_3$ axes, where $\sigma_1$ is WNW-NW-trending and $\sigma_3$ is ENE-NE-trending. The El Tofo Structural System is compatible with a transtensional regime during its early stage and a transpressional regime during its late stage. The Intermediate Structural System shows an EW-shortening axis and NS-extension axis, with both transpressional-transtensional solutions.

## 4. Methodology

Samples included fresh and unfractured host rock, damage zones and fault cores in order to be representative of the fault zone architecture and of the Fe-Cu paragenetic mineral assemblages (e.g. Gudmundsson et al., 2010; Faulkner et al., 2010). A total of 31 samples were collected from surface at North and South Dominga, including 2 oriented samples from North Dominga and 4 from South Dominga, and 25 non-oriented samples collected from six diamond drill holes. Finally, to visualize the spatial distribution of fault cores and damage zones, six detailed structural sections (1:20 scale and ~400 m long; Fig. 1c, d) were built parallel to the azimuth of each drill hole, covering depths from 100 and 850 m (DN11-136, DN12-185, DS11-134, DS11-147, DS11-165, DS12-231).

Microstructure and mineral observations are presented in terms of ore type and according to the mineralization stage to which they belong. Veins and breccia bodies were described based on geometry, internal structure (e.g. syntaxial, composite veins) and infill mineral texture (e.g. massive, blocky, elongate-blocky). The terminology of breccia and vein microstructure for gangue minerals (e.g. quartz) is based on the classification of Oliver and Bons (2001) and Moncada et al, (2012) (and references therein) whereas that regarding ore mineral textures is based on Craig (2001) and Taylor (2009). Logged mineral grain size was grouped into coarse (> 5 mm), medium (1–5 mm), fine (0.1–1 mm) and very-fine (< 0.1 mm).

Microstructural and texture observations were obtained by using an optical transmitted and reflected polarized light microscope and Scanning Electron Microscope with Energy-Dispersive X-ray spectroscopy (SEM-EDX) and cathodoluminescence (CL) (Quanta 250, SEM-CL laboratory of the CEGA-Department of Geology, Universidad de Chile). Doubly-polished thin sections (31) were prepared for petrography, texture and crystal morphology observations on transparent and opaque minerals. To visualize the 3D shape of crystals, thin sections of samples obtained from drill holes were made horizontal and vertical to the vein wall, as the state of stress is strike-slip dominated. Considering mineral assemblages, microstructural observations were conducted on nine samples from the early Fe Stage, eight samples from the late Fe Stage, and eight from the early Cu Stage (Stages according to Veloso et al., 2017).

For this study, we focused on representative textures of veins and hydrothermal breccias of the early and late Fe mineralization stage, as well as the early Cu mineralization stage of the Dominga deposit. The late Cu mineralization stage was not considered for this study due to the low volume of ore.

In order to measure three-dimensional paleo-permeability anisotropy of the Early Fe mineralization stage (one episode of fracturing), numerical fluid flow simulations were carried out through the Lattice-Boltzmann Method (LBM) according to Gomila et al. (2018) and Molina et al. (2019).

Three dimensional structural data were obtained through X-ray micro-computed tomography (microCT). Based on X-ray attenuation, microCT images distinguish differences in the density of the components of rock samples, which are shown in grayscale (e.g. matrix vs. ore minerals; Bultreys et al., 2016). Images were acquired from two microCT equipment at the International Geothermal Centre (GZB) at the Bochum University of Applied Science, Germany, and at the Department of Chemistry and Bioprocesses at the Pontificia Universidad Católica de Chile (PUC), Chile.

For an accurate image acquisition, the calibration for dense minerals (e.g. magnetite, pyrite) was 115 KV, 140 μA, exposure time 350 ms, copper filter 0.5 mm thin and pixel size 8.10 μm at the GZB, and 100 KV, 100 μA, exposure time 2000 ms, aluminum filter 0.1 mm thin and pixel size 5.46 μm at the PUC. We analyzed two oriented surface samples collected at South Dominga: sample DG0102 (vein hosted in diorite and disseminated magnetite, Fig. 3a) and sample DG0206 (vein and disseminated Fe-rich layers hosted in volcaniclastic rocks, Fig. 3b). For each, we prepared an oriented micro-drilling core (5 and 10 mm in diameter and 30 mm long, respectively). After image acquisition, in order to analyze different ore occurrences and geometry separately (e.g. layers from vein segmentation), raw images were processed using open-source softwares (ImageJ© and ITK-SNAP©) and Matlab© scripts (supplementary Fig. 1). Since our samples include

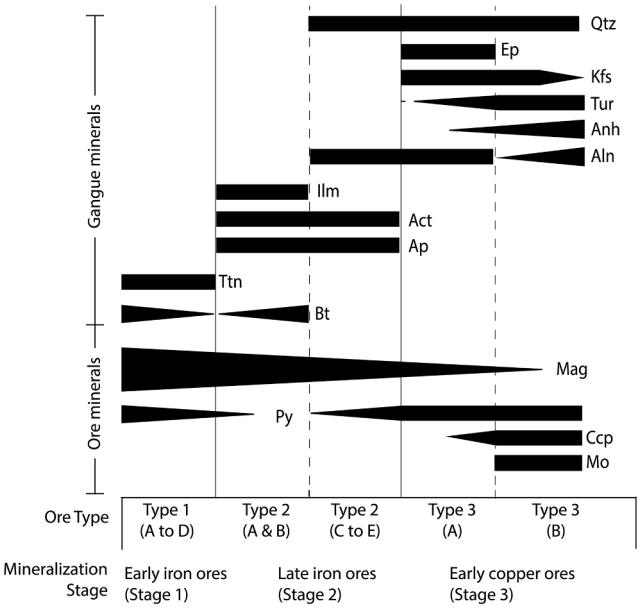


**Fig. 2.** Paragenetic mineral assemblages and ore type of the mineralization stages of the deposit. Relative abundance of minerals is indicated by triangles and rectangles (After Veloso et al., 2017).

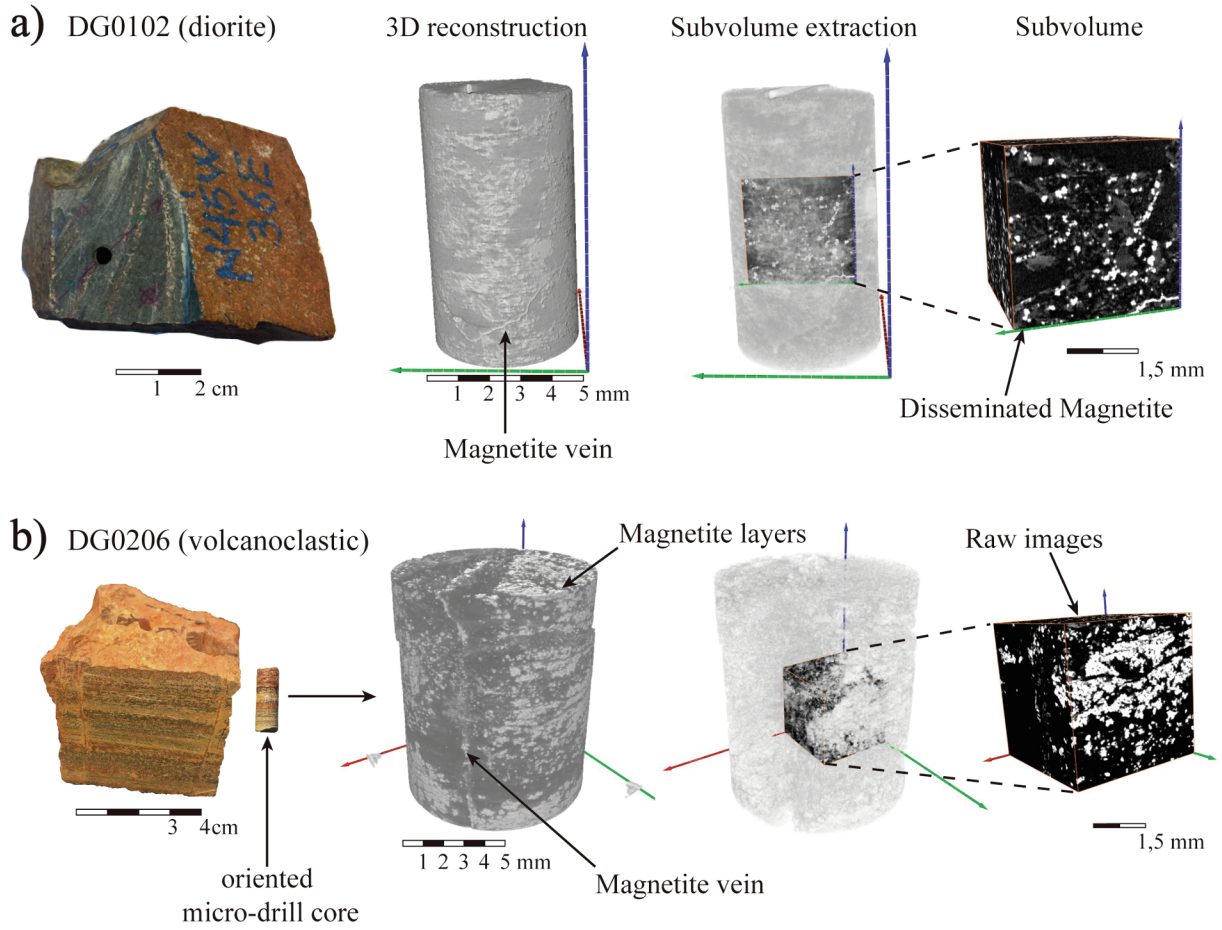


**Fig. 3.** Data acquired from microCT scanning. a Diorite and b Volcaniclastic rock. Data are presented from left to right as follows: 1) Hand sample and micro drill-core. 2) 3D volume reconstruction, composed of approximately 1200 single images. Different components of each rock (e.g. matrix, ore minerals) denoted in grayscale according to their attenuation coefficient (density). Green and red axis horizontal (x and y direction, respectively), blue axis vertical (z-direction). 3) Representative subvolume selection. 4) Raw images of a subvolume. Each subvolume is then filtered, binarized and segmented (discretized) for fluid-flow modeling. (For interpretation of the references to colour in this figure legend, the reader is referred to the web version of this article.)

magnetite and pyrite in the same paragenetic mineral assemblage, it is not necessary to separate those mineral phases. Filters were applied to reduce artifacts and noise (e.g. Anisotropic Diffusion, Median filter, respectively), and for accurate recognition of features between the components of the samples (e.g. boundaries). Based on morphological operations (e.g. Doube et al., 2010), the processed 3D-volume (vertical composes approx. 1200 slices/images) is then segmented into binary images where the discretized space for modeling is isolated. After the segmentation process, the volume is divided into representative sub-volumes (Keehm and Mukerji, 2004; Videla et al., 2008), which contain the pore/fracture network to be modeled (Fig. 3, supplementary Fig. 1). Permeability is reasonably determined when the length of the digital rock (L) is greater than 10 characteristic length scales of the fracture (a) ($L \geq 10a$). For both analyzed samples (DG0102 and DG0206) representative sub-volumes are 500 × 500 × 500px (Fig. 3). The segmented sub-volume is submitted to numerical fluid flow simulations through the LBM which simulates the fluid transport through the pore and/or fracture network space in three directions (x, y, z) in order to evaluate permeability anisotropy (e.g. Faulkner and Armitage, 2013).

The basic concept of LBM corresponds to particles which propagate (e.g. "crush") to a neighboring lattice point, depending on their velocity and initial position, and collide with each other, in such a way that momentum is conserved, which means that on a binary (segmented) image, the particles will propagate only when they find a neighbor with the same value (value 1, otherwise 0). Conversely, if the particle propagates into a neighbor with value zero (0) the particle will rebound and will propagate in another direction. For this purpose, we used the D3Q19 scheme for three-dimensional Lattice Boltzmann simulations (supplementary Fig. 2).

The LBM is based on Darcy's law.

$$\frac{Q}{A} = \frac{k}{\mu}\frac{Pi - P0}{L}$$

where Q is the flow rate transported through pore space, A is the cross-sectional area of the sample, $P_0$ and $P_i$ are the fluid pressure in the outlet and in the inlet of the sample respectively, μ is the dynamic viscosity of the fluid, L the length of the medium, and k the permeability of the sample. We used the open source software Palabos and a parallel Lattice Boltzmann Solver to simulate fluid flow through fractures. The Palabos software provides us with permeability as a function of the velocity magnitude ($v$) of the flow described by expression:

$$k = \frac{\frac{\mu < v >}{dP}}{dL}$$

## 5. Results

### 5.1. Ore types

Based on the paragenetic mineral assemblages identified by Veloso et al, (2017), Dominga ores may be grouped into early and late iron ores, and early copper ores.

*5.1.1. Early iron ores (Stage 1)*

Early iron ores crop out throughout Dominga and have been additionally identified down to 450 m depth with a general envelope up to 30 m thick, parallel to the bedding in volcano-volcaniclastic rocks and parallel to fault cores in diorite. The early iron ores are composed of magnetite, pyrite and biotite as breccias (type 1A, Fig. 4a), veins (type 1B, Fig. 4b, e), layers (type 1C, Fig. 4b, c, d, e) and disseminated ores (1D, Fig. 4f). In general, early iron ores share similar mineral textures and their shapes are anhedral to subhedral unless stated otherwise.

Type 1A ores represent < 3.5 m thick breccia bodies present at the borders of foliated, subvertical ultracataclasite zones oriented N30-50E (Fig. 5a), and are restricted to diorites. These breccias contain subangular to locally rounded clasts of diorite up to 1.5 cm wide within a matrix of fine-grained magnetite and medium-grained pyrite. Commonly, massive pyrite is set in geometry compatible with dilational jogs (Fig. 6a, b, c). Type 1B ores represent vein zones up to 7 m wide, composed of laterally stacked veins dominantly oriented N30-50 W and subordinately oriented N30-50E, parallel to 1A ores. Individual veins are < 1.5 mm thick and are mostly composed of fine to very fine-grained massive to blocky magnetite (Fig. 6d, e, f) and fine-grained pyrite. Type 1C ores are layered zones up to 0.5 m thick comprised of multiple < 5 mm thick, massive stacked layers, parallel to east-dipping bedding of volcaniclastic rocks (Fig. 5b). Layers of this ore type are connected to one and other by 1B veins (Figs. 4b, 6d) and are predominantly made up of very-fine grained, pervasive-disseminated anhedral magnetite and very-fine grained to coarse-grained pyrite. Type 1D ores comprise zones of very fine to fine-grained, disseminated ore minerals with various thicknesses, generally bordering zones of other ore types. There is usually a spatial association between 1D, 1B, and 1C ore types, possibly attesting to a genetic relationship.

*5.1.2. Late iron ores (Stage 2)*

Late iron ores only crop out in South Dominga but have been identified throughout the deposit at depths between 120 and 200 m. These ores share a common mineral assemblage including magnetite, pyrite and actinolite. Accessory mineral assemblages, spatial distribution and infill mineral textures can be used to distinguish two groups of late iron ores.

The first group of late iron ores, types 2A and 2B, has only been found in South Dominga and is represented by breccia bodies and veins (Table 1). Type 2A ores are represented by vertical breccia bodies up to 5 m thick whereas type 2B ores are veins concentrated within 3 m thick zones flanking 2A ores (Figs. 5d; 7a). Although ores 2A and 2B occur spatially together, 2B ores lack preferential orientation with respect to the 2A ores. Both ore types are composed of medium to coarse-grained euhedral magnetite (Fig. 8a, b, d) and fine to coarse-grained euhedral

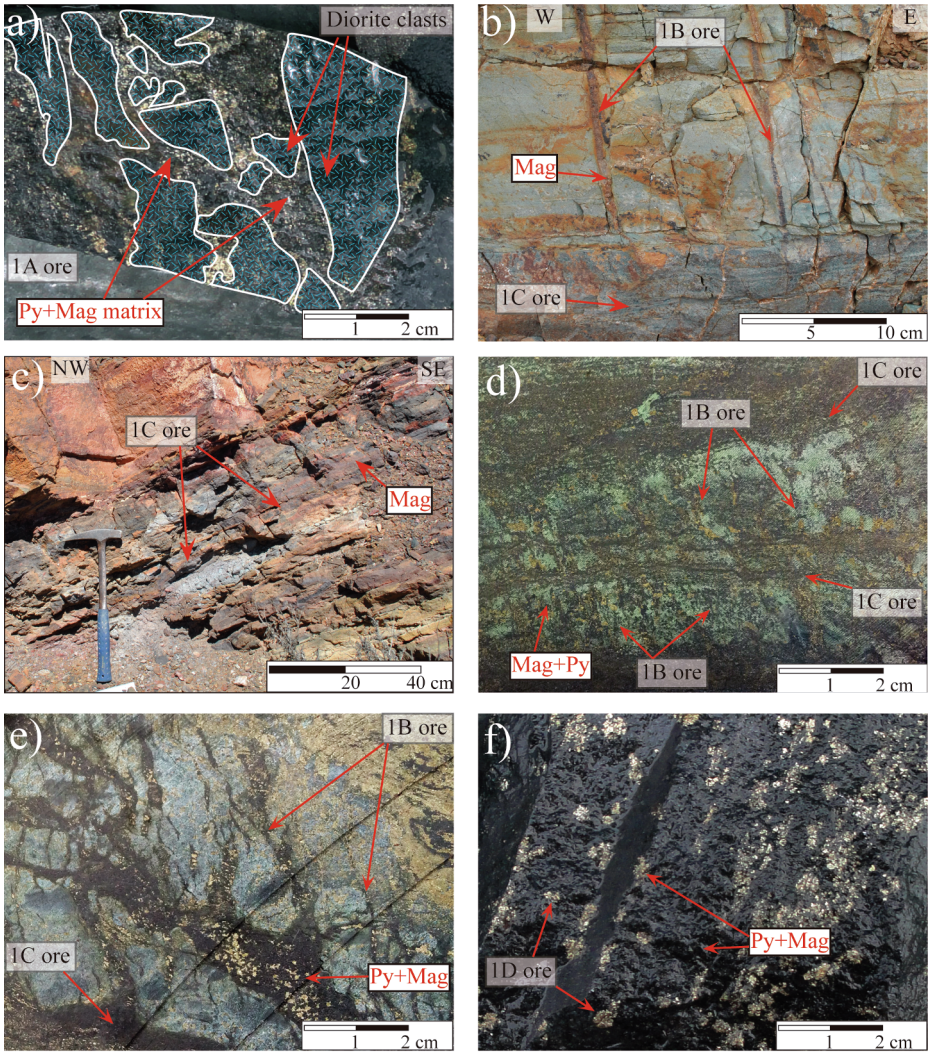


**Fig. 4.** Early iron ores (Stage 1) occurrence. a 1A ore type (breccia) with diorite clasts. b 1B ore type (vein) connected to 1C ore type (layers). It is possible to distinguish ore-rich zones and ore-poor zones. c 1C ores emplaced in east-dipping volcaniclastic rocks. It is possible to distinguish ore-rich zones and ore-poor zones. d Layers (1C ore) connected through millimetric veins (1B ores). e 1B ore connected to 1C ore. f 1D ore.

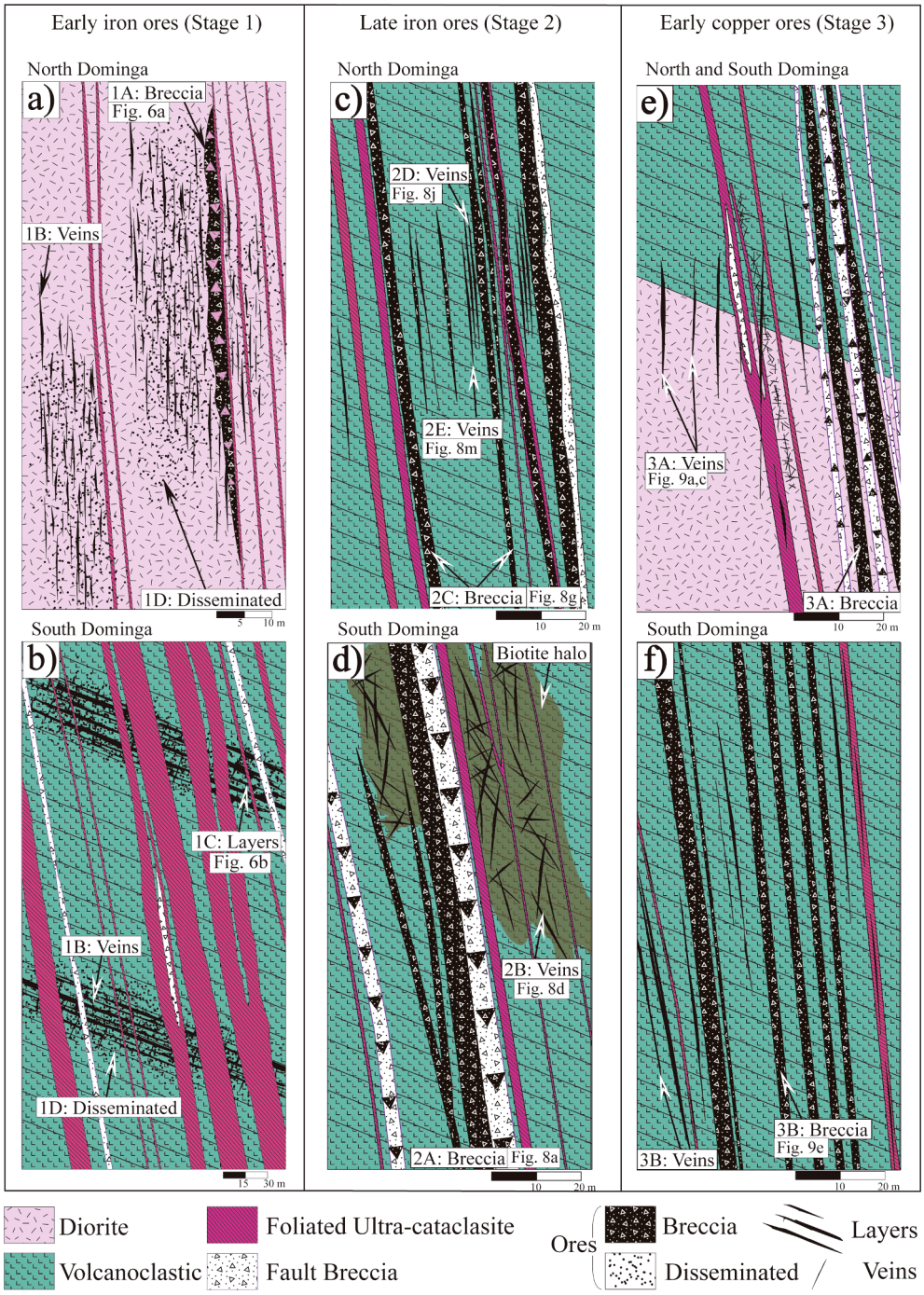


**Fig. 5.** Schematic vertical structural sections showing Dominga ore types. (a, b) early iron ores in north and south Dominga respectively. (c, d) late iron ores in north and south Dominga respectively. (e, f) early copper ores in north and south Dominga. Triangles within breccias represent cross-cutting relationships. Location of representative samples indicated. Veins are not to scale.

and zoned actinolite. Subordinate minerals include medium-grained, anhedral apatite and subhedral biotite. The distinguishing features of 2A and 2B ores are abundant lamellae ilmenite exsolutions in magnetite (Fig. 8c, f) and the spatial association with a disseminated biotite ( ± magnetite) halo (Fig. 8d). Type 2B vein ores have complex internal structures which are not present in 2A breccias, including blocky magnetite perpendicular to the vein wall that forms a syntaxial vein structure (Fig. 8e). Additionally, very fine-grained, elongate, late-stage biotite and quartz are hosted between magnetite grains, but they are also elongated perpendicular to the vein wall forming an ataxial structure (e.g. Bons et al., 2012).

The second group of late iron ores, types 2C, 2D and 2E, is restricted to North Dominga (Fig. 5c) and can also be divided into breccia ores (2C, Fig. 8g) and vein ores (2D and 2E, Fig. 8j, m). Type 2C ores are emplaced as < 5 m thick breccia bodies following a general N30-50Wstrike whereas type 2D ores consist of multiple < 1.5 cm thick veins forming zones up to 5 m thick, bordering 2C ores. Thus, 2D vein ores mostly follow the N30-50W strike, but some isolated veins are subordinately hosted along a N30-50E trend. Type 2E veins are spatially distal to 2C and 2D breccia zones and their orientation is unknown. These three ore types share medium-grained pyrite and coarse-grained actinolite. Subordinate minerals include medium-grained

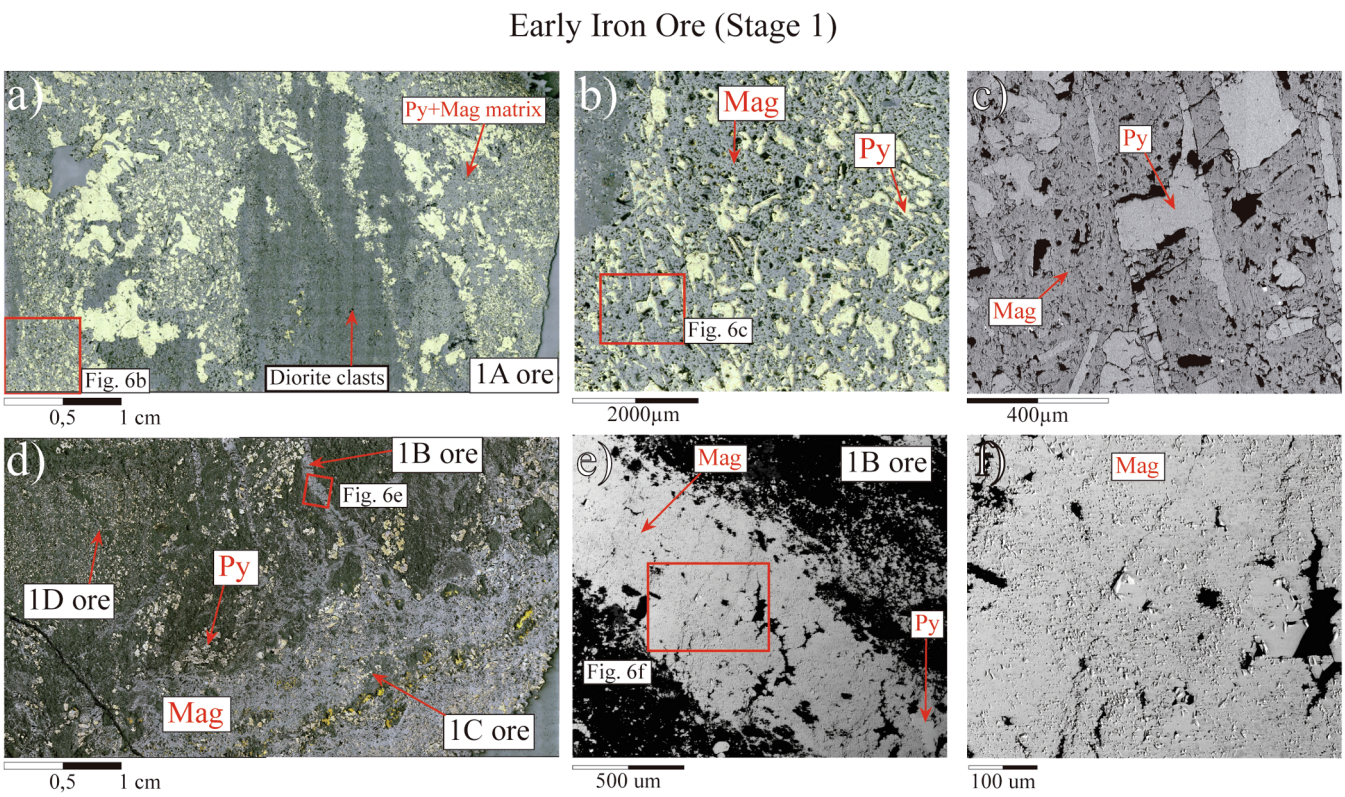


**Fig. 6.** Early iron ores textures and internal structure. a Scanned thin sections of 1A ore breccia composed of magnetite + pyrite matrix and subangular to rounded diorite clast. Reflected light. (b-c) Photomicrograph and SEM-BSE image of detail in 6a (red rectangle) of dilational jog filled with massive pyrite. c Scanned thin sections of 1B, 1C and 1D. Spatial relationship between these ore types in volcaniclastic rocks. Layers (1C) are connected to veins (1C), 1D ore bordering 1C and 1B ores. Reflected light. (e-f) SEM-BSE image of detail in 6d shows vein filled with mostly anhedral magnetite (massive) vein and local subhedral (blocky) texture. Mag: magnetite, Py: pyrite. (For interpretation of the references to colour in this figure legend, the reader is referred to the web version of this article.)

euhedral quartz, medium to coarse-grained magnetite, coarse-grained anhedral apatite and medium-grained euhedral zoned allanite. Excepting apatite and magnetite, minerals in both 2C and 2D show growth zoning. Type 2E vein ores have similar mineralogy, but they lack apatite and quartz and growth zoning. As in the description of the first group, type 2D and 2E veins can have complex mineral textures and internal structures that are not present in type 2C breccias. In type 2D ores, quartz shows double-terminated shapes (Fig. 8k) and growth zoning perpendicular to the C-axis, marked by concentric inclusion trails (Fig. 8l). This double-terminated was observed in thin sections parallel and vertical to the vein wall. Often, quartz can be overgrown by concentric plumose quartz (Fig. 8l). Type 2E ores, on the other hand, lack quartz, but show fibrous actinolite oriented oblique to the vein walls, forming an antitaxial vein structure (Fig. 8m, n, o).

### 5.1.3. Early copper ores (Stage 3)

Early copper ores crosscut all previous Fe-rich ores (Fig. 7b) and crop out only in South Dominga, however they have been identified throughout the deposit between 80 and 950 m of depth. Ores from this stage are generally emplaced along the foliation planes of N50-80E striking, dextral, S-C ultracataclasites which locally exhibit strike-slip duplex-like geometry compatible with sinistral kinematics (Fig. 7c). Copper ores have a distinct mineral assemblage with only chalcopyrite and accessory magnetite, potassic feldspar and tourmaline (Table 1). Main mineral assemblage and spatial distribution can be used to distinguish between two groups of early copper ores.

The first group of early copper ores, type 3A ores, are emplaced both in South and North Dominga as breccia bodies (< 5 m thick) and veins (< 3 cm thick). Their mineral assemblage includes quartz, pyrite and chalcopyrite as main minerals with potassic feldspar, allanite, epidote, magnetite and tourmaline as accessories. Unlike ore types from other stages, veins are emplaced with no clear spatial relation to breccia bodies.

Type 3A breccia is composed of fine-grained to coarse subhedral pyrite, fine-grained anhedral magnetite, and fine-grained blocky quartz. Type 3A vein ores have complex inner structures which are not present in 3A breccias. These include a combination of three different quartz textures (Fig. 9a) in a syntaxial vein structure: 1) adjacent to the vein wall as very-fine grained elongate-blocky quartz, 2) towards the vein center showing epitaxial growth from its neighbor as fine to medium-grained elongate-blocky quartz, and subhedral medium-grained epidote, and 3) in the center of veins as very-fine grained subhedral blocky quartz associated with anhedral chalcopyrite (Fig. 9b). Type 3A veins also include infill minerals such fine-grained subhedral microcline exhibiting growth zoning and granophyric texture (Fig. 9c, d). These types of veins exhibit syntaxial internal structure.

The second group of early copper ores, type 3B, occurs only in South Dominga and is represented by both breccia bodies (< 5 m thick) and veins (2–5 mm thick) of unknown orientation. These ores form zones up to 60 m thick, and they are emplaced deeper in the deposit (from 300 to 950 m) in comparison with 3A. These ores are characterized by their assemblage of anhydrite, gypsum, chalcopyrite and accessory potassic feldspar, magnetite, allanite, tourmaline and molybdenite. Ore type 3B (breccia and veins) are composed of fine to medium-grained euhedral anhydrite (Figs. 9e, 10c), very fine-grained anhedral chalcopyrite intergrown with anhedral allanite, medium to coarse-grained subhedral tourmaline, very-fine grained subhedral molybdenite and very-fine grained anhedral magnetite. Type 3B breccias and veins exhibit a syntaxial inner structure defined by the zone adjacent to the vein wall as medium-grained blocky euhedral anhydrite showing optical continuity, and in the center of the breccias, an inner assemblage of fine-grained, blocky anhedral anhydrite. Subordinate chalcopyrite, pyrite,

**Table 1**
Summary of ore type mineralogy, occurrence, geometry, internal structure and mineral texture.

| Mineralization Stage | Ore Type | Occurrence | Main Mineralogy | Accesory Minerals | Geometry | Vein Structure | Mineral Texture |
|---|---|---|---|---|---|---|---|
| Early iron ores (Stage 1) | 1A | Breccia | mag + py + bt | ttn | Vertical | | Massive |
| | 1B | Vein | mag + py + bt | ttn | Vertical | | Massive, blocky |
| | 1C | Layer | mag + py + bt | ttn | Bedding-parallel | | Massive |
| | 1D | Disseminated | mag + py + bt | ttn | | | Massive, blocky |
| Late iron ores (Stage 2) | 2A | Breccia | mag + py + act ± ap | bt | Vertical | | blocky, Ilmenite exsolution |
| | 2B | Vein | mag + py + act ± ap | bt ± qz | No preferential orientation | Syntaxial, ataxial | blocky, Ilmenite exsolution, elongate |
| | 2C | Breccia | py + act ± ap + mag | qz + aln | Vertical | | Qz: blocky, double terminated, plumose |
| | 2D | Vein | py + act ± ap + mag | qz + aln | Vertical | | Qz: blocky, double terminated |
| | 2E | Vein | py + act ± mag | | Vertical | Antitaxial | fibrous |
| Early copper ores (Stage 3) | 3A | Breccia and Vein | qz + py ± ccp | kfs + ep + mag + tur + aln | Vertical | Syntaxial | blocky, elongate-blocky, granophyric |
| | 3B | Breccia and Vein | anh + ccp | mag + kfs + mo + aln + tur | Vertical | Syntaxial | blocky |

magnetite and molybdenite are present in both the inner and outer parts of the breccia (Fig. 9f).

### 5.2. Paleo-permeability of early iron ores

The bulk of ores in Dominga belongs to the early iron ore stage (1A to 1D), thus identifying permeability in associated structures and lithologies (e.g. diorite and volcaniclastic) is of paramount importance to understand how metallogenetic processes generated this resource. An important parameter that needs to be addressed in this effort is how fluids percolated through primary and/or structural permeability during the creation of these ores. In order to determine the role of rock permeability and consequent fluid migration on the genesis of Dominga early iron ore types, we measured the paleo-permeability anisotropy of one sample of 1C layered ores, as a proxy for primary permeability, as well as samples of two 1B veins, which represent structural permeability. Considering that the type of permeability might have a role in the mechanisms of ore precipitation, by for example controlling the abundance of ore minerals in relation to a given type of permeability, we measured the proportional abundance of ore types in a representative segment of Dominga associated with the Early Structural System.

Sample DG0206 is a dominantly 1C ore hosted in volcaniclastic rock with ~15% disseminated ore minerals as layers and 3.7% as vein ore minerals. Separate fluid flow simulations were performed in three directions (parallel to the principal stress axis $\sigma_1$, $\sigma_2$, and $\sigma_3$) in each ore type to allow for a comparison of their paleo-permeability. Fluid flow simulations of layered ore show a high value of permeability parallel to layers ($K_{Hx} = 7.22 \times 10^{-11}$ and $K_{Hy} = 6.01 \times 10^{-11}$; Fig. 11a), although vertical permeability is also present, albeit one-order of magnitude lower ($K_{Vz} = 3.73 \times 10^{-12}$). Also, vertical permeability exhibits multiple paths (not distinguishable on thin sections) between layers (Fig. 11a). Fluid flow simulations on vein ore show the highest value in the vertical direction (parallel to $\sigma_2$; $K_{Vz} = 5.54 \times 10^{-12}$; Fig. 11b) whereas horizontal permeability is two-orders of magnitude smaller ($K_{Hy} = 8.20 \times 10^{-14}$). Horizontal paleo-permeability ($K_{Hx}$) was not measured due to a lack of connectivity between the vein and the boundaries of the sub-volume, a condition that is required in order to obtain a permeability value through fluid flow simulation (Degruyter et al., 2010).

Sample DG0102 is a dominantly 1D ore hosted in diorite with ~4% disseminated ore minerals and ~1.5% vein ore minerals. Fluid flow simulations of this sample were performed in relation to the vein and show that the highest value of permeability is parallel to the vertical direction (parallel to $\sigma_2$; $K_{Vz} = 9.8 \times 10^{-13}$) whereas horizontal permeability is $4.62 \times 10^{-14}$ and $1.40 \times 10^{-13}$ ($K_{Hx}$ and $K_{Hy}$ respectively). Even though horizontal permeability is low, the paleo-permeability represented by 1B veins is connected to the paleo-permeability represented by disseminated mineralization (Fig. 11c).

## 6. Discussion

Microstructural observations and numerical fluid flow simulations evidence a causal relationship between tectonic (structural systems), mineralization emplacement (Fe-Cu bearing-fluids migration) and host rock permeability. The interaction of these factors determines the occurrence of ores through mass transfer mechanisms that follow the primary and structural permeability of host rocks (e.g. Bense et al., 2013), the type of flow (e.g. advection vs diffusion, Hilgers et al., 2004; Okamoto and Tsuchiya, 2009; Oliver and Bons, 2001), episodes of fault activity (e.g. crack-seal mechanism) and variations on stress condition associated with fault zone architecture (e.g. fault valve, suction pump mechanism, e.g. Sibson, 2004). The development of various mineral textures and structures in vein-related mineralization is interpreted as being caused by changes in the tectonic regimes that indicate: 1) variation of fluid flow direction related to multiple crack-seal episodes, 2)

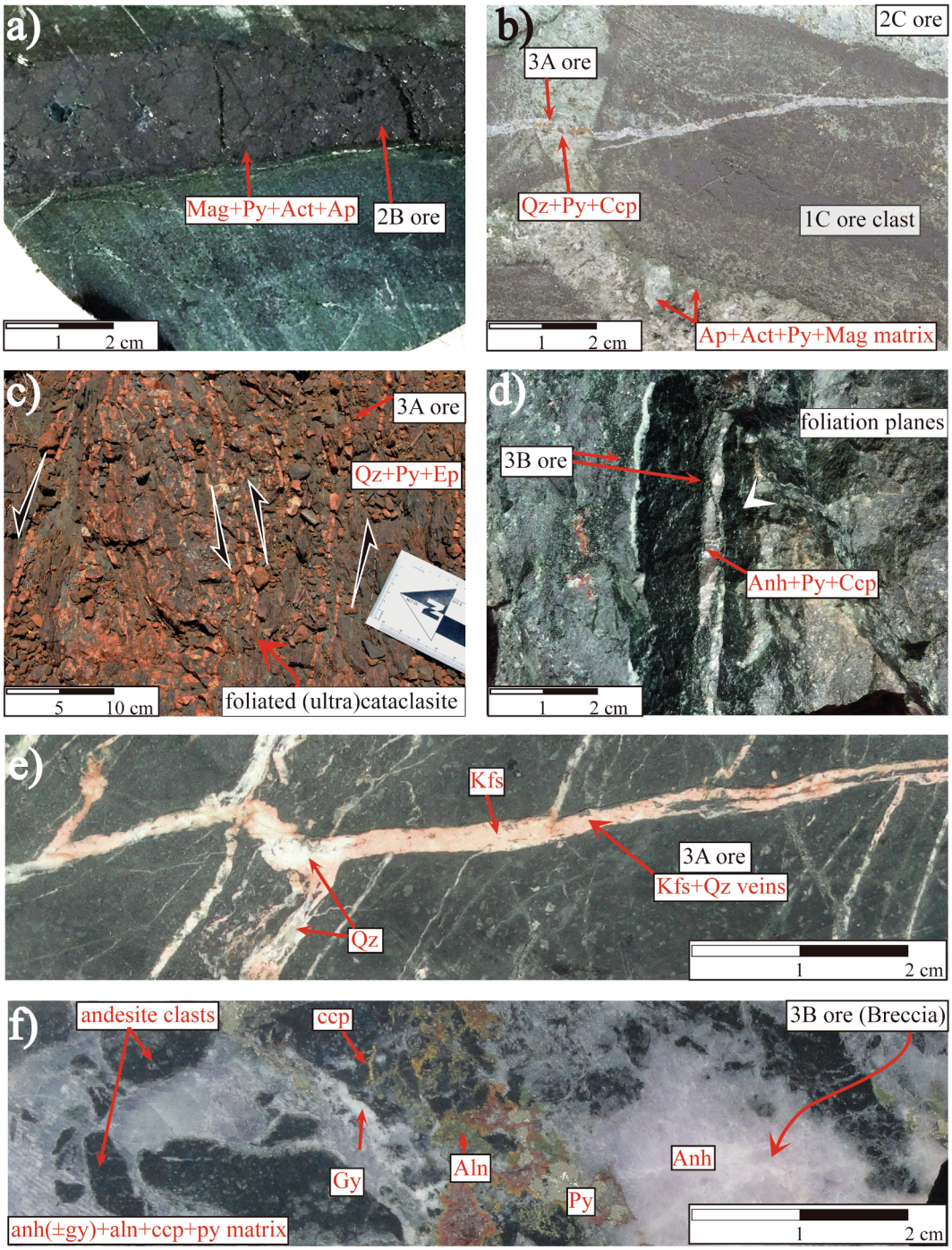


**Fig. 7.** Late iron ores (Stage 2) and Early copper ores (Stage 3) occurrence. (a, b) Late iron ores and (c-e) early copper ores. a 2B ore: magnetite + pyrite + actinolite + apatite vein. b Cross-cutting relationship between 1C ore (clast of layered ores), 2C ore (breccia) and 3A ore (vein), from oldest to youngest respectively. c 3A ore: quartz + k-feldspar veins emplaced in foliation planes of dextral (ultra)cataclasite. Veins are organized according to a sinistral strike-slip duplex geometry (plan view). d 3B ore: anhydrite + pyrite + chalcopyrite vein in foliation planes of (ultra)cataclasite (belonging to the Early Structural System). e 3A ore: k-felldspar + quartz veins, 3B ore: anhydrite + chalcopyrite rich-matrix breccia. Anh: anhydrite, Aln: allanite, Ccp: chalcopyrite, Ep: epidote, Gy: gypsum, Kfs: k-feldspar, Mag: magnetite, Py: pyrite. Qz: quartz.

multiple modes of fracture opening (e.g. mode I, mode II, mode III, Scholz, 2002). In contrast, disseminated Fe-rich layers seem to be more closely related to bedding-parallel fluid flow associated with intergrain porosity while only maintaining a subordinate relationship to a vertical, fault-related control. Therefore, the optimal window for iron mineralization is determined by the interaction of the primary and structural permeability of volcaniclastic rocks, both associated with advective Fe-rich fluids.

### 6.1. Genesis of Early iron ores

Based on kinematic data and the spatial relationships between faults, Veloso et al. (2017) interpreted that fracturing related to the Early Structural System in the Dominga deposit is characterized by NE-ENE and NW oriented fault zones generated under a transtensional regime. On diorites, (ultra)cataclasites belonging to the Early Structural System are flanked by breccias 1A, veins 1B and disseminated 1D type.

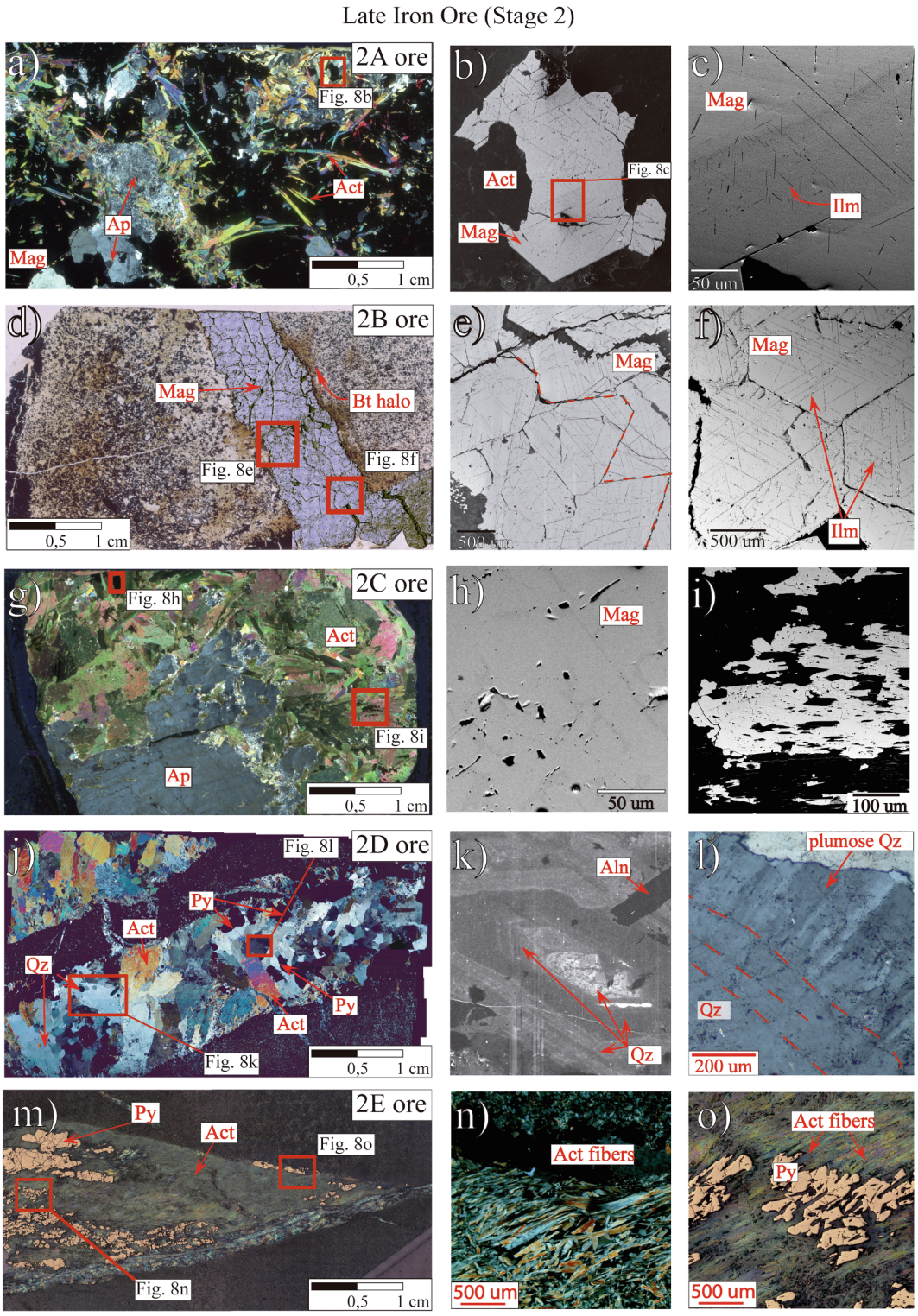


**Fig. 8.** Late iron ores textures and internal structure. a Scanned thin section of 2A ore breccia (cross polarized). b-c SEM-BSE images of detail of magnetite crystal in 8a (red rectangle) with ilmenite lamellae exsolution. d Scanned thin section of 2B ore syntaxial magnetite vein with biotite halo (reflected light). e-f SEM-BSE images of detail of magnetite crystal in (8d) showing euhedral coarse-grained octahedral magnetite crystals with ilmenite lamellae exsolution. Suture zone can be distinguished (red dashed line). g Scanned thin section of 2C ore breccia (cross polarized). h-i SEM-BSE images of detail of magnetite crystal in (8 g). Anhedral coarse-grained magnetite with no exsolution texture. j Scanned thin section of 2D ore vein (cross polarized). k SEM-CL image of euhedral quartz crystals which exhibit growth zoning and double terminated shape. l Photomicrograph of zoned quartz surrounded by plumose quartz (cross polarized). m Scanned thin section of 2E ore actinolite antitaxial vein (reflected light). n Actinolite fibers oblique to the vein wall (cross polarized). o Actinolite fibers intergrown with pyrite (reflected light). Act: actinolite, Aln: allanite, Ap: apatite, Bt: biotite, Ilm: ilmenite, Mag: magnetite, Py: pyrite. Qz: quartz. (For interpretation of the references to colour in this figure legend, the reader is referred to the web version of this article.)

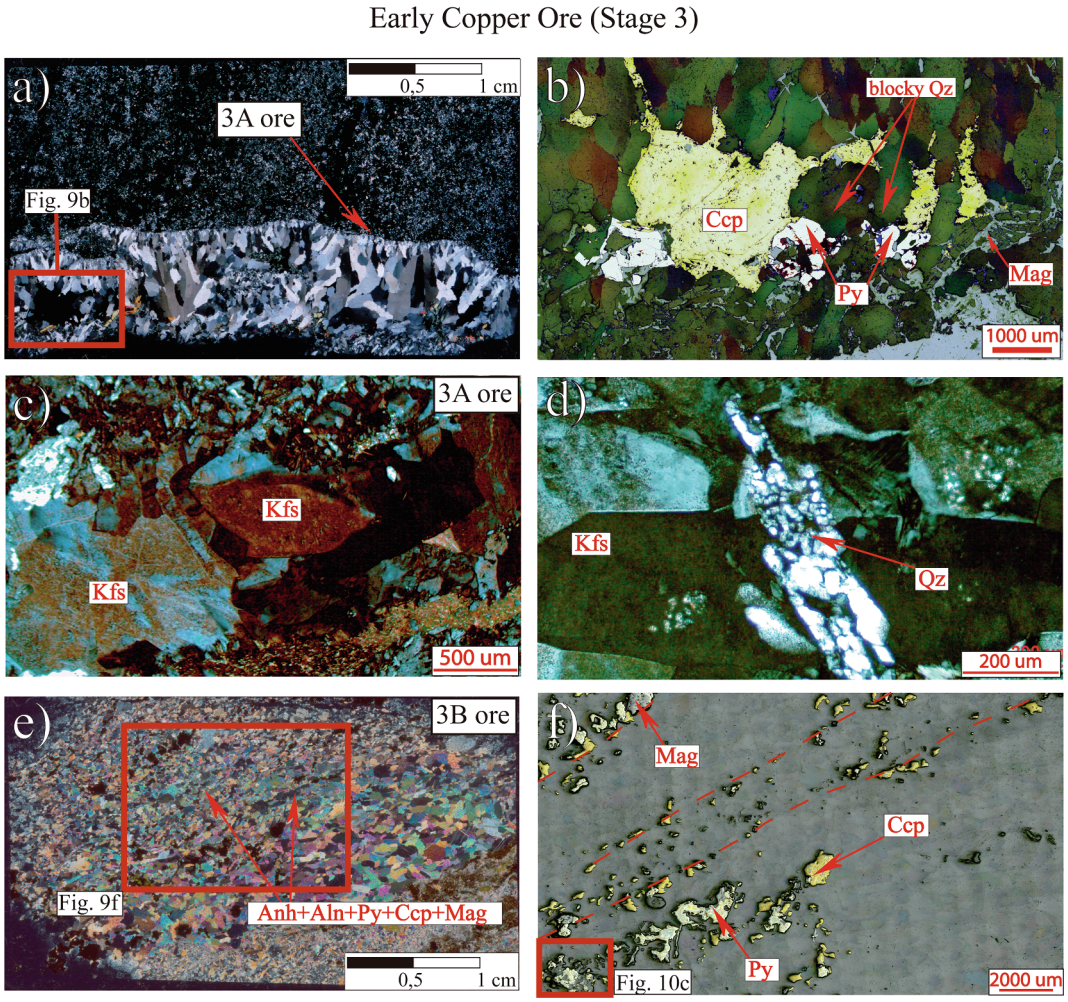


**Fig. 9.** Early coper ores textures and internal structure. a Scanned thin section of 3A ore vein with syntaxial internal structure (cross polarized). Quartz crystals exhibit three types of mineral textures: fine-grained elongate-blocky on the vein wall, elongate-blocky and blocky at the center (cross polarized). b Photomicrograph of image detail in 9a (red rectangle). Chalcopyrite associated with blocky quartz at the center of vein (reflected light, PPL). c Photomicrograph of 3A ore vein (cross polarized). d Photomicrograph of K-feldspar with granophyric exsolution texture (cross polarized). e 3 Scanned thin section of 3B ore breccia with syntaxial internal structure (cross polarized). f Photomicrograph of detail in 9e (red rectangle). Ore minerals aligned and intergrown with anhedral allanite (reflected light). Anh: anhydrite, Aln: allanite, Ccp: chalcopyrite, Kfs: k-feldspar, Mag: magnetite, Py: pyrite. Qz: quartz. (For interpretation of the references to colour in this figure legend, the reader is referred to the web version of this article.)

Spatial relationships and ore distribution (Figs. 10a, 12a) between breccias, veins and disseminations can be explained by local variations in differential stress conditions. According to Cosgrove (1995), the orientation of tensile fractures (mode I) becomes more random as the differential stress ($\sigma_1$–$\sigma_3$) decreases towards zero and generates brecciation. Releasing bends and dilational jogs are favorable sites for this stress condition (e.g. Bons et al., 2012). Adjacent to these breccia 1A zones, where differential stress is different than zero ($\sigma_1$–$\sigma_3 \neq 0$), vertical fractures with similar directions could form. The latter can be observed in the spatial relationship between the fault core, represented by (ultra)cataclasites, and the damage zone which hosts proximal early iron ore breccias 1A and distal 1B veins. Thus, (ultra)cataclasites, breccias, and veins could have all been generated under a single deformation/mineralization event associated with the Early Structural System. Fractures and breccias generated in this early event created secondary permeability through which mineralized-fluids could flow.

Additional evidence of transtension and mineralizing-fluid flow is given by massive pyrite filled dilational jogs within 1A breccia (Fig. 6c). Such geometry and texture may suggest mineral precipitation from an advective flow (Beach and Jack, 1982) through either a suction pump mechanism (e.g. Sibson, 1994), differential stress close to zero (Cosgrove, 1995) and/or fast sealing (Passchier and Trouw, 2005). In volcaniclastic rocks, internal structure, massive to blocky texture and the crystal shape of 1B ores suggest a single episode of fracturing (one crack-seal episode) and fast fracture sealing through the fault valve mechanism (e.g. Sibson, 1994) that propagates an advective fluid flow. Moreover, since the geometric relationship between 1C layers and 1B veins was observed from the outcrop scale down to a millimetric scale, it is plausible to think that a channelized fluid flow through the thicker magnetite veins and a pervasive fluid flow through micro veins (e.g. Oliver and Bons, 2001) could act together as a path for an advective flow, as a main mass transfer mechanism (Figs. 10a, 12a). Channelized fluids circulating through magnetite veins are likely to spread out laterally in permeable horizons to form 1C layers. These interpretations may prompt fluid flow mechanisms related to the early iron ores to occur at the same time, under stress conditions that vary locally from the fault core to the damage zone.

The multiple geometries of early iron ores can be explained by the structural plumbing system and the interaction between primary and structural permeability of diorites and volcaniclastic rocks rather than by multiple episodes of Fe-rich fluid migration. Under a transtensional regime, fractures likely develop maximum permeability anisotropy in the vertical direction (following $\sigma_2$) and parallel to $\sigma_1$ (maximum horizontal) (Faulkner and Armitage, 2013). Hence, numerical fluid flow

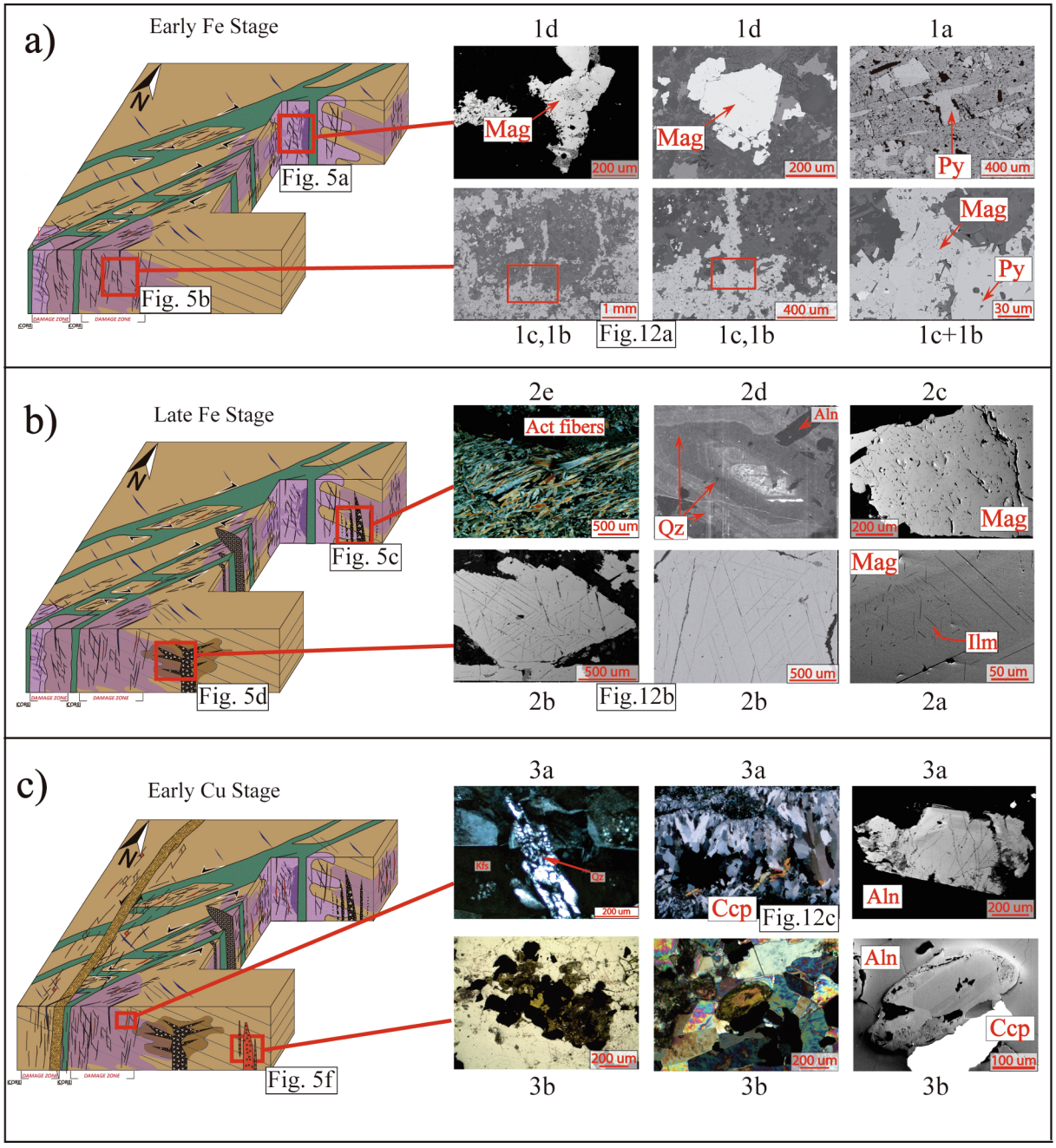


**Fig. 10.** Distribution and spatial relationship between Ore Types in the Dominga Fe-Cu deposit and a summary of their textures. a Spatial relationship between Early Iron Ores. In north Dominga, hosted by diorites, 1A ore breccia body is located at the borders of fault cores and flanked by 1D ore disseminated subhedral magnetite. In south Dominga, hosted by volcaniclastic rocks, 1B and 1C ores are connected. This spatial relationship was observed from the outcrop scale down to millimetric/micrometric length scale. b Spatial relationship between Late Iron Ores. In north Dominga, 2C ore breccia body is flanked by 2D and 2D ore types. These ore types have the same mineral assemblage; however, different textures are observable. In south Dominga, 2A ore type is surrounded by 2B ore type. Both ore types exhibit Ilmenite exsolution lamellae. c Early Copper Ores. Syntaxial 3A veins show three quartz texture from the vein wall to the vein center. Chalcopyrite is associated with blocky quartz at the center of the vein. Anh: anhydrite, Aln: allanite, Ccp: chalcopyrite, Kfs: k-feldspar, Mag: magnetite, Py: pyrite. Qz: quartz.

simulation on 1B veins emplaced in diorite and volcaniclastic rocks are consistent with the permeability anisotropy expected for a transtensional regime ($K_{Vz} \approx K_{Hy} > K_{Hx}$), similar to those of the intermediate stress axis described by Veloso et al. (2017). However, numerical fluid flow simulation on 1C layers ($K_{Hx} \approx K_{Hy} > K_{Vz}$) suggests that the main control on fluid flow is related to primary permeability. Nevertheless, the subvertical orientation of the minimal permeability axis ($K_{Vz}$) from rock layering matches the tectonic regime as well, suggesting that this small component represented by multiple paths along the vertical direction (Fig. 11a) is controlled by the local regime rather than the primary permeability features. Such paths could be interpreted as micro veins that act as a connector between 1C layers similar to those 1B veins observed on the outcrop scale down to thin section (Figs. 4b, 6b, 10a). This demonstrates that the structural permeability likely plays a key role in mineralizing-fluid migration at several length scales through a vertical channelized and pervasive fluid flow mechanism. Conversely, fluid flow simulation on diorite 1B vein show that this ore is connected to 1D ore (disseminated) suggesting a genetic relationship between these ore types and that 1B veins represent feeders of Fe bearing-fluids which fill microfractures as disseminated ores (1D ore, Figs. 10c, 11a).

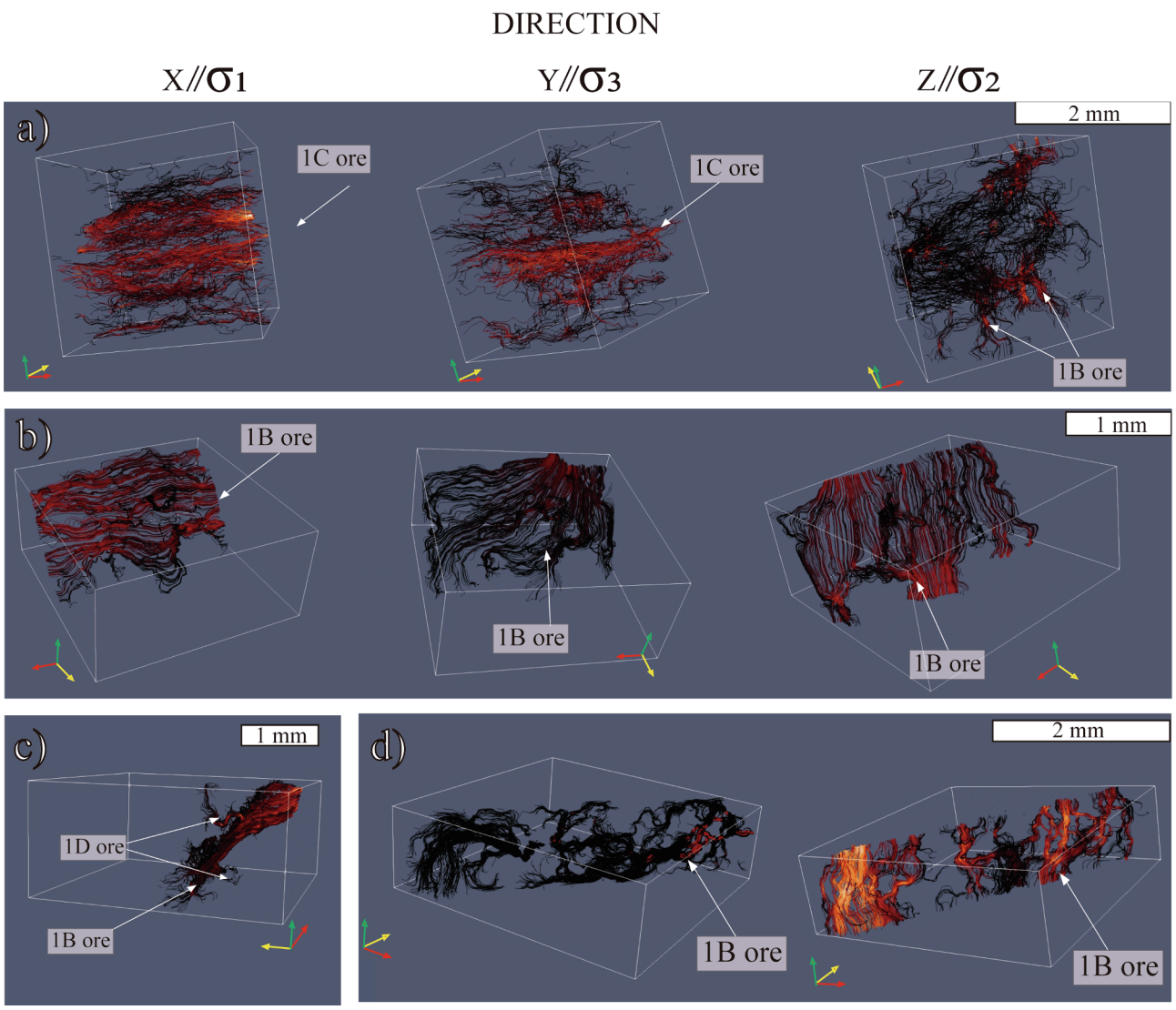


**Fig. 11.** Numerical fluid flow simulation results. a 1C layered ore hosted in volcaniclastic rock (sample DG0206). Permeability is higher in horizontal direction (*x* and *y* parallel to σ1 and σ3, respectively) than vertical direction (*z* parallel to σ2). Layers are connected between them through fluid paths along *z*-direction. b 1B vein in diorite (sample DG0102). c 1B vein locally connected to disseminated mineralization (Sample DG0102). d 1B vein in volcaniclastic rock (sample DG0206). Warm colors indicate higher permeability. Red axis: horizontal *x* direction, yellow axis: horizontal *y* direction, green axis: vertical *z* direction. (For interpretation of the references to colour in this figure legend, the reader is referred to the web version of this article.)

The interpretations that prompt the Fe bearing-fluids to be emplaced on diorite are purely fault-controlled. Additional evidence from ore modal abundance of 1C (layers)/1D (disseminated) vs 1B vein ores, suggest that primary permeability (bedding concordant/parallel) is a more favorable site than fracture for ore precipitation and that fractures are a better plumbing system than bedding. However, the occurrence of early iron ores is controlled by both primary and structural permeability, which act together.

Marshick and Fontboté (2001) suggest that the iron oxide stage (magnetite) in the Candelaria-Punta del Cobre deposits (Iron Oxide Copper-Gold type) was structurally controlled by fault zones. Here, subvertical ore bodies reached permeable horizons, and fluids spread out laterally to form concordant ore bodies. However, fluids were focused by north-west striking faults, whereas at the Dominga deposit, fluids associated with the Early Iron Ores are genetically related to north-east- to east-north-east striking fault zones (Early Structural System).

### 6.2. Genesis of late iron ores

According to Veloso et al. (2017), the occurrence of parallel NW-striking breccias and veins and their spatial relationship can be explained by a tensional position of fractures with respect to the Early Structural System (parallel to $\sigma_1$), whereas fractures with no preferential orientation (e.g. 2B vein) may suggest a differential stress close to zero ($\sigma_1$-$\sigma_3 \approx 0$).

Fractures and breccias generated in this late iron episode created secondary permeability through which fluids could flow. This can be observed in the spatial and cross-cutting relationship between fault cores, represented by (ultra)cataclasites, as well as in damage zones which host late iron ore breccias 2A and 2C, distal 2B and 2D veins and marginal 2E veins.

In south Dominga, 2A breccia and 2B veins that share common textures, for example, the presence of ilmenite lamellae exsolution in magnetite of 2A breccia (Figs. 5d, 8b) and ilmenite lamellae exsolution texture in magnetite of 2B veins (Figs. 5d, 8e) suggest a common origin between those elements. Additional evidence of these elements having the same origin can be observed in their spatial relationship, where 2B

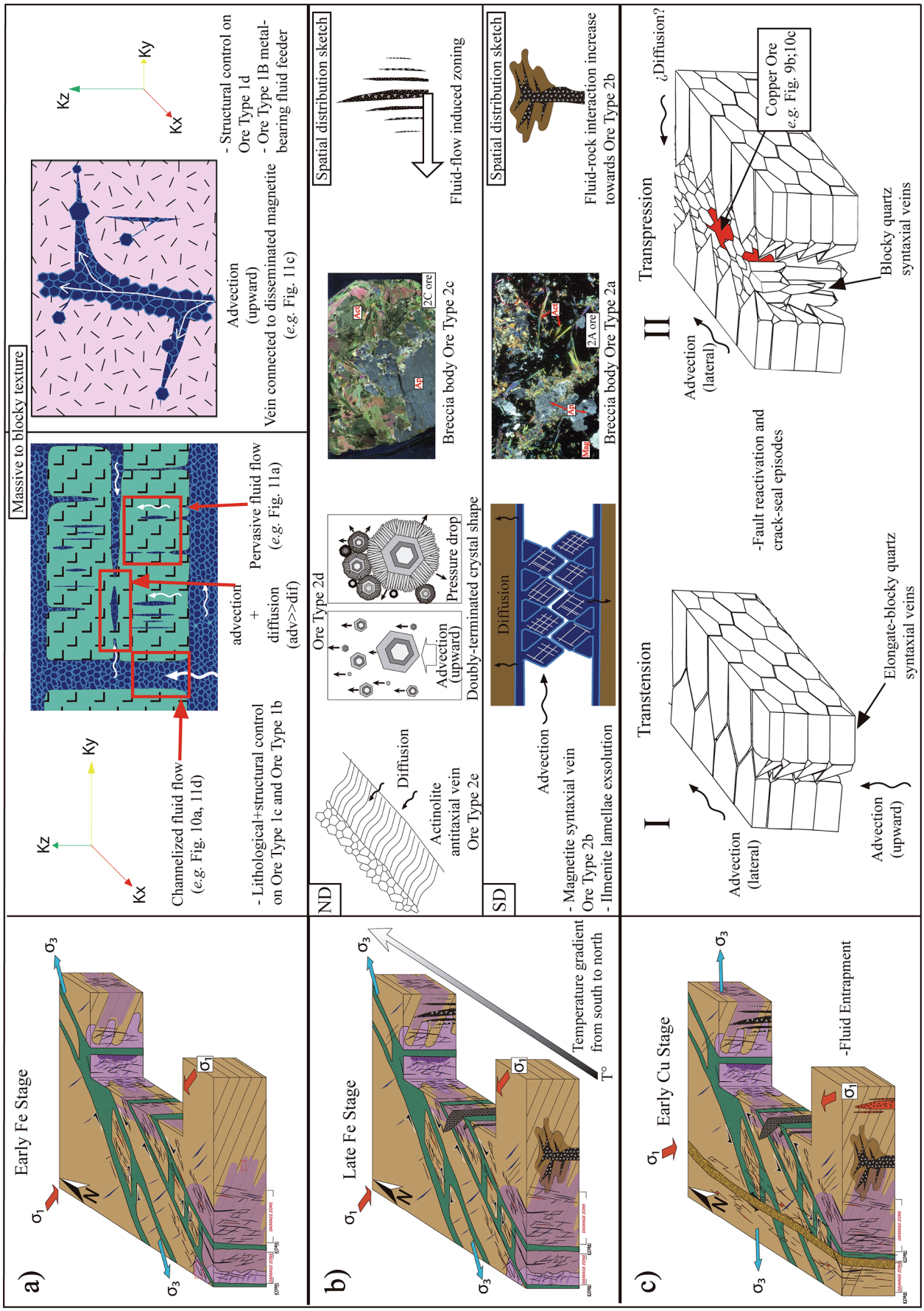


*(caption on next page)*

**Fig. 12.** Integrated conceptual model for inferring fluid-flow mechanisms at the Dominga Fe-Cu deposit, based on ore distribution, textures, and the measured permeability anisotropy (Early iron ores). a relationship between permeability anisotropy and the occurrence of early iron ores related to the Early Structural System. Magnitude of permeability axis (red, yellow and green) according to their value for 1C ore (left, $K_{Hx} \approx K_{Hy} > K_{Vz}$) and 1B ore (right, $K_{Vz} \approx K_{Hy} > K_{Hx}$), b emplacement of hydrothermal breccia from an advective flow and later boiling, Temperature gradient from South to North Dominga. c episodes of fault zone reactivation (Early Structural System) related to the early activity of the El Tofo Structural System. Syntaxial vein (3A) with textures suggesting several crack-seal episodes; the last episode is associated with chalcopyrite mineralization under a transpressional regime. ND: north Dominga, SD: south Dominga. (For interpretation of the references to colour in this figure legend, the reader is referred to the web version of this article.)

veins lack preferential orientation with respect to the 2A breccia. These may be interpreted as stable hydrofractures (Bons, 2001; Oliver and Bons, 2001). Since stable hydrofractures involve brecciation and random orientation of fractures at the top, fluid-rock interaction is favored. Hence, biotite haloes related to 2B veins may be developed due to a diffusional fluid flow controlled by a pressure gradient (Fig. 12b).

In contrast, in north Dominga, quartz with doubly-terminated shape (e.g. 2D vein, Fig. 8k) suggests a continuous crystallization from an aqueous advective fluid with enough energy to balance the downward crystal settling and keep the crystals in suspension (Okamoto and Tsuchiya, 2009). Plumose quartz occurs as concentric structures (e.g. hydrothermal coatings) around such double terminated quartz crystals. They may indicate a late change in fluid conditions that could be associated with a pressure drop and boiling (Moncada et al., 2012; Shimizu, 2014) during a late episode of fluid migration. The spatial relationship between 2C and 2D ores (breccia and vein), as well as quartz crystals with a doubly-terminated shape are interpreted to have formed as mobile hydrofractures (e.g. Bons, 2001; Oliver and Bons, 2001). Distal fibrous actinolite antitaxial veins (2E veins, Fig. 8m) support a decrease in the opening rate of fractures (Hilgers et al., 2001; Passchier and Trouw, 2005) at a relatively low strain rate during the interseismic period (e.g. Power and Tullis, 1989). These veins are interpreted as the boundary of the breccia-veins system (2C-E ores), a decrease in the capability of fractures related to the Early Structural System to propagate mineralizing-fluids, and a fluid-flow induced zoning (Figs. 10b, 12b).

Similar paragenetic mineral assemblage, spatial orientation and distribution of 2A-B ores in relation to 2C-E ores are interpreted as different parts of the same episode of fluid flow. Abundant Ilmenite lamellae exsolutions texture found on magnetite from the late iron ores (2A breccia and 2B veins) support the hypothesis of a hydrothermal origin and establish a crystallization temperature higher than 600 °C (Tan and Liang, 2016, and references therein) and a temperature gradient from south to north Dominga. The idea of a temperature gradient is also supported by mineral zonation where quartz and pyrite content in north Dominga argue for a more differentiated fluid.

Additionally, magnetite exhibiting Ilmenite lamellae exsolution texture is described at some Iron Oxide Apatite deposits within the CIB, for example, El Romeral, Los Colorados, Cerro Negro Norte, and Carmen (Rojas et al., 2018; Knipping et al., 2015; Salazar et al., 2019; Palma et al., 2019, respectively). Based on trace element distribution in magnetite (e.g. Ti, V, Mn, Al), the authors suggest a high-temperature hydrothermal origin for magnetite of massive breccia bodies. Paragenetic mineral assemblages and textural similarities between those mineralizing episodes and late iron ores (2A and 2B) present at the Dominga Fe-Cu deposit argue for a similar origin and condition of the fluid.

We argue that fluid flow mechanisms involved in the precipitation of early and late iron ores can be considered as evidence of different processes related to fluid migration and conditions of mineralizing-fluids during the main activity and abandonment of the Early Structural System, related to the change in the orientation of the principal stress axes ($\sigma_1$, $\sigma_2$, $\sigma_3$) and the tectonic regime (e.g. Veloso et al., 2017).

### 6.3. Genesis of Early copper ores

According to Veloso et al. (2017), the change in the tectonic regime from transtensional to transpressional could reactivate the elements of the Early Structural System, but with sinistral kinematics, thus inducing the transition from the Fe stage to the Cu stage of mineralization. Field observations on a duplex like geometry composed of 3A veins (Fig. 7*c*) argue for a fault zone reactivation because the duplex geometry is compatible with sinistral kinematics (as the El Tofo Structural System), however 3A veins are emplaced within foliation planes of dextral (ultra)cataclasites with S-C texture of the Early Structural System.

The abandonment of the Early Structural System and the early stages of the El Tofo Structural System resulted in fluid entrapment, evidenced by the development of granophyric texture (Fig. 9*d*) in 3A veins indicating crystallization from aqueous fluid under slow cooling conditions (Deer et al., 1998; Klein and Philpotts, 2013; Vernon, 2017). The main activity of the El Tofo Structural System for this stage is characterized by 3A syntaxial veins (Fig. 9*c*) and 3B breccia. The internal structure of 3A veins (Fig. 9*a*) and the mineral texture related to each episode of fracturing are interpreted to have formed from: 1) crack-seal episodes, and 2) advective flows with different directions. Veins attributed to the crack-seal mechanism (Ramsay, 1980; Wiltschko and Morse, 2001) are commonly considered as evidence for episodic crack opening driven by fault reactivation (often related to the fault-valve mechanism (e.g. Oliver and Bons, 2001), whereas internal structures, such as the combination of mineral textures represent single and/or multiple episodes of fracturing. This suggests a reuse of fractures by fluids of a different composition. According to Hilgers et al. (2004) elongate-blocky crystals may grow from an advective flow and perpendicular to the flow direction (Fig. 12c).

In fault zones, the high permeability direction is developed parallel to the intermediate principal stress axis ($\sigma_2$) (Sibson, 1994; Cox, 2005; Rowland and Simmons, 2012). Here, we propose that mineral textures related to the internal structure of composite veins, from elongate-blocky crystals on the vein wall to blocky crystals towards the center may be interpreted as crystallization from advective (and locally diffusive?) fluids, propagated in different directions due to fracturing under different tectonic regimes through the crack-seal mechanism.

The emplacement of 3B breccia during the main activity of the El Tofo Structural System may indicate a progressive decrease in the flow rate towards the center of the breccia body (3B). This is evidenced by gradation in the size of blocky anhydrite crystals from coarse-grained on the wall to fine-grained towards the center. This suggest that anhydrite and chalcopyrite initially precipitated under a high-opening rate from a high-flow advective flow (Hilgers et al., 2001; Hilgers and Urai, 2002a,b; Hilgers et al., 2004; Woodcock et al., 2007) to a lower opening and flow rate.

## 7. Conclusions

1) Ores at the Dominga Fe-Cu deposit occur as breccia bodies, veins, and disseminated-rich layers developed under multiple tectonic regimes. Fluid flow mechanisms related to each episode of fluid migration and ore deposition involve local variations on the stress condition and opening mode of fracture, associated with the spatial distribution of early iron ores concerning the architecture of the Early Structural System (e.g. proximal/distal to the fault core or damage zone). Internal structure and the development of different mineral textures depend on the type of flow-mass transfer (e.g. advection), fluid flow direction (accordingly to the tectonic regime),

the number of episodes of fracturing/sealing (e.g. fault zone reactivations), and local variations in the condition of the fluid (e.g. pressure drop).

2) Each ore type shows different combinations of fluid flow mechanisms. Geometry, mineral texture and numerical fluid flow simulation on Early iron ores argue for fluid flow mechanisms related to: fault-valve, suction-pump, and advective-pervasive flow. Late iron ores exhibit evidence of fluid flow mechanisms related to: fault-valve, advection, local diffusional fluid flow and temperature gradient from south (> 600 °C) to north. Early copper ores exhibit evidence of fluid flow mechanisms related to: fault-valve, advection and crack-seal mechanisms. These variations of flow mechanisms indicate that they can operate at the same time and that they are independent of the tectonic regime.
3) Numerical fluid flow simulations support a genetic relationship between Early iron ores; permeability anisotropy argues for a lithological and structural control on their occurrence. In dioritic rocks, the emplacement of iron ore zones was controlled by the development of 1B veins, which would have acted as fluid feeders of Fe-rich advective flow related to tensile and/or hybrid fractures (tension + shear). Whereas in volcaniclastic rocks, the permeability anisotropy of 1B veins and 1C layers is compatible with that of a transtensional regime. These ore type are controlled by the primary permeability but with a structural permeability component that allows 1B veins to occur between layers at several length scales.
4) Permeability anisotropy and ore modal abundance suggest that primary permeability of stratified rocks is a more favorable site for ore precipitation, and that fractures are a more efficient plumbing system. The optimal window for Iron mineralization is controlled by the interaction of primary and structural permeability in volcaniclastic rocks, both associated with advective Fe bearing-fluids. Therefore, volcaniclastic rocks gather both permeability conditions to host economic Fe-Cu deposits. However, diorite fracture-hosted ores are a useful target for exploring Fe-Cu.
5) The spatial distribution and mineral texture of ore types indicate that ore-related fluid flows at the Dominga Fe-Cu deposit were highly heterogeneous even in the same structural element and/or geometric arrangement. This is observed in 3A syntaxial veins, which, although they were developed under a single tectonic regime, show textural elements such as elongate-blocky quartz on the vein wall, elongate-blocky quartz and blocky quartz at the center of vein, textures which are compatible with changes in the fluid flow direction.
6) The main difference between iron and copper ores fluid flow mechanisms is the greater number of episodes of fluid migration associated with early copper ores and fault reactivation when compared to the Fe stage.
7) 3A ore type at the Dominga Fe-Cu deposit suggest a complex history of mineral growth and microstructural evolution representing the transition and reuse of previous structural elements. Textures and mineral assemblages indicate that the main fluid flow mechanism corresponds to advective fluid flow through crack-seal episodes, suggesting different conditions during mineral precipitation, from aqueous fluid (on early iron-copper stages) to (possibly) episodic boiling (on late iron ores). The development of different textures related to composite veins could represent at least two fluid flow directions, and therefore, textures likely recorded episodes of fault reactivations and fluid propagation under different tectonic settings.

## Acknowledgments

This work is a contribution to the Millennium Nucleus for Metal Tracing Along Subduction NC 130065. We would like to thank Andes Iron SpA and Iván Garrido for granting access to the Dominga deposit and sampling. The authors would like to thanks to Dr. Huayong Chen and anonymous reviewers. Their comments and suggestions helped to highly improve the quality of the manuscript. We acknowledge the International Geothermal Centre (GZB) (Bochum, Germany) for facilities and technical assistance of the Geothechnologies and Seismic Observation Laboratories and Fondequip project EQM 130028 (microCT-PUC). CONICYT-Ph.D. Scholarship N°21171021 has funded tuition and some operational costs of GH.

## Appendix A. Supplementary data

Supplementary data to this article can be found online at https://doi.org/10.1016/j.oregeorev.2020.103316.

## References

Arévalo, C., Grocott, J., Martin, W., Pringle, M., Taylor, G., 2006. Structural setting of the Candelaria Fe oxide Cu-Au deposit, Chilean Andes (27°30′S). Econ Geol 101, 819–841.
Beach, A., Jack, S., 1982. Syntectonic vein development in a thrust sheet from the external French Alps. Tectonophysics 81, 67–84.
Bense, V.F., Gleeson, T., Loveless, S.E., Bour, O., Scibek, J., 2013. Fault zone hydrogeology. Earth Sci. Rev. 127, 171–192. https://doi.org/10.1016/j.earscirev.2013.09.008.
Bons, P.D., 2001. The formation of large quartz veins by rapid ascent of fluids in mobile hydrofractures. Tectonophysics 336, 1–17.
Bons, P.D., Elburg, M.A., Gomez-Rivas, E., 2012. A review of the formation of tectonics veins and their microstructures. J. Struct. Geol. 43, 33–62.
Bonson, C., Grocott, J., Rankin, A., 1996. A structural model for the development of Fe-Cu mineralization within the Atacama Fault System, (25°00′S–27°15′S), Northern Chile. Third ISAG, St. Malo, France, pp. 671–674.
Brown, M., Diaz, F., Grocott, J., 1993. Displacement history of the Atacama Fault System 258009–278009S, northern Chile. Geol. Soc. Am. Bull. 105, 1165–1174.
Bultreys, T., De Boever, W., Cnudde, V., 2016. Imaging and image-based fluid transport modeling at the pore scale in geological materials: a practical introduction to the current state-of-the-art. Earth. Rev. 155, 93–128. https://doi.org/10.1016/j.earscirev.2016.02.001.
Cembrano, J., Garrido, I., Marquardt, M., 2009. Tectonic setting of IOCG deposits in the Central Andes: Strike-slip-dominated deformation. XII Congreso Geológico Chileno, Santiago: S9_043.
Chen, H., Cooke, D.R., Baker, M.J., 2013. Mesozoic iron oxide copper-gold mineralization in the Central Andes and the Gondwana supercontinent breakup. Econ Geol 108, 37–44.
Creixell, C., Arévalo, C., 2009. Geología del Cuadrángulo El Tofo, Región de Coquimbo. SERNAGEOMIN, Gobierno Regional de Coquimbo. 1 mapa a escala 1:50.000.
Coira, B., Davidson, J., Mpodozis, C., Ramos, V., 1982. Tectonic and magmatic evolution of the Andes of northern Argentina and Chile. Earth Sci. Rev. 18 (3–4), 303–332.
Cosgrove, J., 1995. The expression of hydraulic fracturing in rock and sediments. From Ameen, M.S (ed), 1995, Fractography: fracture topography as tool in fracture mechanics and stress analysis. Geological Society Special Publication No. 92, pp. 187-196.
Cox, S.F., 2005. Coupling between deformation, fluid pressures, and fluid flow in ore producing hydrothermal systems at depth in the crust. Econ. Geol. 39–76 100th Anniversary Volume.
Craig, J.R., 2001. Ore-mineral textures and the tales they tell. Can. Mineral. 39, 937–956.
Deer, W.A., Howie, R.A., Zussman, J., 1998. Rock Forming Minerals, 2nd edition. The Geological Society, London. J. Petrol. 39 (6), 1251–1253. https://doi.org/10.1093/petroj/39.6.1251.
Degruyter, W., Burgisser, A., Bachmann, O., Malaspinas, O., 2010. Synchrotron X-ray microtomography and lattice Boltzmann simulations of gas flow through volcanic pumices. Geosphere 6, 470. https://doi.org/10.1130/GES00555.1.
Doube, M., Kłosowski, M.M., Arganda-Carreras, I., Cordeliéres, F., Dougherty, R.P., Jackson, J., Schmid, B., Hutchinson, J.R., Shefelbine, S.J., 2010. BoneJ: free and extensible bone image analysis in ImageJ. Bone 47, 1076–1079. https://doi.org/10.1016/j.bone.2010.08.023.
Espinoza, S., 1984. Le rôle du Crétacé inférieur dans la métallogénèse de la ceinture ferrifère d'Atacama-Coquimbo, Chili: Unpublished doctoral thesis, Paris, l'Université Pierre et Marie Curie, Paris, 153 p.
Espinoza, S., 1990. The Atacama-Coquimbo ferriferous belt, northern Chile. In: Fontboté, L., Amstutz, G., Cardozo, M., Cedillo, E., Frutos, J. (Eds.), Stratabound Ore Deposits in the Andes. Springer –Verlag, Berlin, pp. 353–364.
Faulkner, D.R., Mitchell, T.M., Rutter, E.H., Cembrano, J., 2008. On the structure and mechanical properties of large strike-slip faults. Geol. Soc., London, Special Publ. 299 (1), 139–150. https://doi.org/10.1144/SP299.9.
Faulkner, D.R., Mitchell, T.M., Jensen, E., Cembrano, J., 2011. Scaling of fault damage zones with displacement and the implications for fault growth processes. J. Geophys. Res. 116, B05403. https://doi.org/10.1029/2010JB007788, 2011.
Faulkner, D.R., Jackson, C.A.L., Lunn, R.J., Schlische, R.W., Shipton, Z.K., Wibberley, C.A.J., Withjack, M.O., 2010. A review of recent developments concerning the structure, mechanics and fluid flow properties of fault zones. J. Struct. Geol. 32, 1557–1575.
Faulkner, D.R., Armitage, P.J., 2013. The effect of tectonic environment on permeability development around faults and in the brittle crust. Earth Planet. Sci. Lett. 375, 71–77.

https://doi.org/10.1016/j.epsl.2013.05.006.
Fossen, H., Tikoff, B., 1998. Geological Society, London, Special Publications Extended Models of Transpression and Transtension, and Application to Tectonic Extended Models of Transpression and Transtension, and Application to Tectonics. pp. 15–33, https://doi.org/10.1144/GSL.SP.1998.135.01.02.
Geijer, P., 1931. The iron ores of the Kiruna type: Sveriges Geologiska Undersökning, n. C367, pp. 39.
Gelcich, S., Davis, D., Spooner, T., 2005. Testing the apatite-magnetite geochronometer: U-Pb and 40Ar/39Ar geochronology of plutonic rocks, massive magnetite-apatite tabular bodies, and IOCG mineralization in Northern Chile. Geochim. Cosmochim. Acta 69 (13), 3367–3384.
Gomila, R., Arancibia, G., Mery, D., Nehler, M., Bracke, R., Morata, D., 2018. Permeability anisotropy and geometrical properties of sealed-microfractures from micro-CT analyses: An open-source implementation. Micron.
Grocott, J., Taylor, G., 2002. Magmatic arc fault system, deformation partitioning and emplacement of granitic complexes in the coastal cordillera, north Chilean Andes (25°30'S to 27°00'S). J. Geol. Soc. Lond. 159, 425–442.
Gudmundsson, A., Simmenes, T., Larsen, B., Philipp, S., 2010. Effects of internal structure and local stresses on fracture propagation, deflection, and arrest in fault zones. J. Struct. Geol. 32, 1643–1655.
Hilgers, C., Koehn, D., Bons, P.D., Urai, J.L., 2001. Development of crystal morphology during unitaxial growth in a progressively widening vein: II. Numerical simulations of the evolution of antitaxial fibrous veins. J. Struct. Geol. 23, 873–885.
Hilgers, C., Urai, J.L., 2002a. Microstructural observations on natural syntectonic fibrous veins: implications for the growth process. Tectonophysics 352, 257–274.
Hilgers, C., Urai, J.L., 2002b. Experimental study of syntaxial vein growth during lateral fluid flow in transmitted light: first results. J. Struct. Geol. 24, 1029–1043.
Hilgers, C., Dilg-gruschinski, K., Urai, J.L., Dynamik, G.E., 2004. Microstructural evolution of syntaxial veins formed by advective flow. Geology 3, 261–264. https://doi.org/10.1130/G20024.1.
Jensen, E., Cembrano, J., Faulkner, D.R., Veloso, E., Arancibia, G., 2011. Development of a self-similar strike-slip duplex system in the Atacama Fault system, Chile. J. Struct. Geol. 33 (11), 1611–1626. https://doi.org/10.1016/j.jsg.2011.09.002.
Kim, Y.S., Peacock, D.C.P., Sanderson, D.J., 2004. Fault damage zones. J. Struct. Geol. 26 (3), 503–517. https://doi.org/10.1016/j.jsg.2003.08.002.
Keehm, Y., Mukerji, T., 2004. Permeability and relative permeability from Digital Rocks: Issues on Grid Resolution and Representative Elementary Volume. SEG Annual Meeting, Denver, CO, pp. 1654–1657. https://doi.org/10.1190/1.1845147.
Klein, C., Philpotts, A., 2013. Earth Materials: Introduction to Mineralogy and Petrology. Cambridge University Press, Cambridge, UK.
Knipping, J.L., Bilenker, L.D., Simon, A.C., Reich, M., Barra, F., Deditius, A.P., Lundstrom, C., Bindeman, I., Munizaga, R., 2015. Giant Kiruna-type deposits form by efficient flotation of magmatic magnetite suspensions. Geology 43, 591–594.
Marschik, R., Fontboté, L., 2001. The Candelaria-Punta del cobre Iron Oxide Cu-Au(-Zn-Ag) deposits, Chile. Econ. Geol. 96 (2001), 1799–1826.
Mathur, R., Marschik, R., Ruiz, J., Munizaga, F., Leveille, R.A., Martin, W., 2002. Age of mineralization of the Candelaria Fe oxide Cu-Au deposit and the origin of the Chilean iron belt, based on Re-Os isotopes. Econ. Geol. 97 (1), 59–71.
Micklethwaite, S., Sheldon, H.A., Timothy, B., 2010. Active fault and shear processes and their implications for mineral deposit formation and discovery. J. Struct. Geol. 32, 151–165.
Mitchell, T.M., Cembrano, J.M., Fujita, K., Hoshino, K., Faulkner, D.R., Flores, P., Gomila, R., 2017. Fluid Inclusion Evidence of Coseismic Fluid Flow Induced by Dynamic Rupture, PP. 37–45.
Molina, E., Arancibia, G., Sepúlveda, J., Roquer, T., Mery, D., Morata, D., 2019. Digital rock approach to model the permeability in an artificially heated and fractured granodiorite from the liquiñe geothermal system (39°S). Rock Mech. Rock Eng. https://doi.org/10.1007/s00603-019-01967-6.
Moncada, D., Mutchler, S., Nieto, A., Reynolds, T., Rimstidt, J., Bodnar, R., 2012. Mineral textures and fluid inclusion petrography of the epithermal Ag–Au deposits at Guanajuato, Mexico: application to exploration. J. Geochem. Explor. 114, 20–35.
Naranjo, J.A., 1987. Interpretación de la actividad Cenozoica superior a lo largo de la zona de falla Atacama, norte de Chile. Rev. Geol. Chile 31, 43–55.
Taylor, R., 2009. Ore Textures: Recognition and Interpretation. Springer-Verlag, Berlin-Heildeberg, pp. 282.
Thiele, R., Pincheira, M., 1987. Tectónica transpresiva y movimiento de desgarre en el segmento sur de la zona falla Atacama, Chile. Rev. Geol. Chile 31, 77–94.
Okamoto, A., Tsuchiya, N., 2009. Velocity of vertical fluid ascent within vein-forming fractures. Geology 6, 563–566. https://doi.org/10.1130/G25680A.1.
Oliver, N., Bons, P.D., 2001. Mechanisms of fluid flow and fluid–rock interaction in fossil metamorphic hydrothermal systems inferred from vein–wallrock patterns, geometry and microstructure. Geofluids 137–162.
Oyarzún, J., Frutos, J., 1984. Tectonic and petrological frame of the cretaceous iron deposits of North Chile. Mining Geol. 34, 21–31.
Oyarzun, R., Oyarzún, J., Ménard, J.J., Lillo, J., 2003. The Cretaceous iron belt of northern Chile: role of oceanic plates, a superplume event, and a major shear zone. Miner. Deposita 38, 640–646. https://doi.org/10.1007/s00126-003-0359-y.
Palma, G., Barra, F., Reich, M., Valencia, V., Simon, A., Vervoort, J., Leisen, M., Romero, R., 2019. Halogens, trace element concentrations, and Sr-Nd isotopes in apatite from iron oxide-apatite (IOA) deposits in the Chilean iron belt: evidence for magmatic and hydrothermal stages of mineralization. Geochim. Cosmochim. Acta 246 (2019), 515–540.
Parada, M.A., López-Escobar, L., Oliveros, V., Fuentes, F., Morata, D., Calderón, M., Aguirre, L., Féraud, G., Espinoza, F., Moreno, H., Figueroa, O., Muñoz, J., Troncoso, R., Stern, C.R., 2007. Andean Magmatism. In The Geology of Chile (Moreno, T.; Gibbons, W.; editors). The Geological Society, Special Publication 4: 115-146. London.
Park Jr, C.F., 1972. The iron ore deposits of the Pacific basin. Econ. Geol. 67, 339–349.
Passchier, C.W., Trouw, R.A., 2005. Microtectonics. Springer-Verlag, Berlin-Heilderberg, pp. 366.
Power, W.L., Tullis, T.E., 1989. The relationship between slickenside surfaces in fine-grained quartz and the seismic cycle. J. Struct. Geol. 11 (7), 879–893. https://doi.org/10.1016/0191-8141(89)90105-3.
Ramsay, J., 1980. The crack-seal mechanism of rock deformation. Nature 284, 135–139.
Rieger, A., Marschik, R., Díaz, M., Hölzl, S., Chiaradia, M., Akker, B., Spangenberg, J., 2010. The hypogene iron oxide copper-gold mineralization in the Mantoverde District, Northern Chile. Econ Geol 105, 1271–1299.
Rojas, P., Barra, F., Deditius, A., Reich, M., Simon, A., Roberts, M., Rojo, M., 2018. New contributions to the understanding of Kiruna-type iron oxide-apatite deposits revealed by magnetite ore and gangue mineral geochemistry at the El Romeral deposit, Chile. Ore Geol. Rev. 93, 413–435.
Rowland, J.V., Simmons, S.F., 2012. Hydrologic, magmatic, and tectonic controls on hydrothermal flow, Taupo Volcanic Zone, New Zealand: implications for the formation of epithermal vein deposits. Econ. Geol. 107 (3), 427–457. https://doi.org/10.2113/econgeo.107.3.427.
Ruiz, C., Aguirre, L., Corvalan, J., Klohn, C., Klohn, E., Levi, B., 1965. Geología y yacimientos metalíferos de Chile: Instituto de Investigaciones Geológicas [Chile], 386 p.
Ruiz, C., Peebles, F., 1988. Geología, Distribución y Génesis de los Yacimientos Metalíferos Chilenos. Editorial Universitaria, Santiago, pp. 334.
Salazar, E., Barra, F., Reich, M., Simon, A., Leisen, M., Palma, G., Romero, R., Rojo, M., 2019. Trace element geochemistry of magnetite from the Cerro Negro Norte iron oxide – apatite deposit, northern Chile. Miner Deposita. https://doi.org/10.1007/s00126-019-00879-3.
Scheuber, E., Gonzales, G., 1999. Tectonics of the Jurassic-Early Cretaceous magmatic arc of the north Chilean Coastal Cordillera (22°–26°S): a story of crustal deformation along a convergent plate boundary. Tectonics 18 (5), 895–910. https://doi.org/10.1029/1999TC900024.
Scholz, C.H., 2002. The Mechanics of Earthquakes and faulting. Cambridge University Press. Cambridge, UK, pp. 470.
Shimizu, T., 2014. Reinterpretation of Quartz textures in terms of hydrothermal fluid evolution at the Koryu Au-Ag deposit, Japan. Econ. Geol. https://doi.org/10.2113/econgeo.109.7.205.
Sibson, R.H., 2004. Controls on maximum fluid overpressure defining conditions for mesozonal mineralisation. J. Struct. Geol. 26, 1127–1136. https://doi.org/10.1016/j.jsg.2003.11.003.
Sillitoe, R.H., 2003. Iron oxide-copper-gold deposits: an Andean view. Miner Deposita 38 (7), 787–812. https://doi.org/10.1007/s00126-003-0379-7.
Sibson, R.H., 1994. Crustal stress, faulting and fluid flow. Geological Society, London, Special Publications. http://doi.org/10.1144/GSL.SP.1994.078.01.07.
Tan, W., Liang, X.I., 2016. Mineralogy and origin of exsolution in Ti-rich magnetite from different magmatic Fe-Ti oxide-bearing. Canad. Mineral. 54, 539–553. https://doi.org/10.3749/canmin.1400069.
Tosdal, R.M., Richards, J.P., 2001. Magmatic and Structural Controls on the Development of Porphyry Cu ± Mo ± Au Deposits. In: Deformation, Fluid Flow and Ore Deposits (eds Richards J, Tosdal R). Reviews in Economic Geology, 14, 1–24.
Uysal, I.T., Feng, Y., Zhao, J., Bolhar, R., Işik, V., Baublys, Ka., Yago, A., Golding, S.D., 2011. Seismic cycles recorded in late Quaternary calcite veins: geochronological, geochemical and microstructural evidence. Earth Planet. Sci. Lett. 303, 84–96. https://doi.org/10.1016/j.epsl.2010.12.039.
Veloso, E., Cembrano, J., Arancibia, G., Heuser, G., Neira, S., Siña, A., Garrido, I., Vermeesch, P., Selby, D., 2017. Tectono-metallogenetic evolution of the Fe-Cu deposit of Dominga, northern Chile. Miner Deposita 52, 595–620. https://doi.org/10.1007/s00126-016-0682-8.
Vernon, R.H., 2017. Microstructures of deformed rocks. A Practical Guide to Rock Microstructure. https://doi.org/10.1017/CBO9780511807206.006.
Videla, A.R., Lin, C.L., Miller, J.D., 2008. Simulation of saturated fluid flow in packed particle beds – the lattice-Boltzmaan method for the calculation of permeability from XMT images. J. Chin. Inst. Chem. Eng, 39 (2), 117–128. https://doi.org/10.1016/j.jcice.2007.12.002.
Vila, T., Lindsay, N., Zamora, R., 1996. Geology of the Manto Verde copper deposit, northern Chile: a specularite-rich, hydrothermal-tectonic breccia related to the Atacama fault zone. Soc. Econ. Geol. Spl. Publ. 5, 157–170.
Vivallo, W., Díaz, A., Jorquera, R. 2008. Yacimientos metalíferos de la región de Atacama, Escala 1:500.000. SERNAGEOMIN, Carta Geológica de Chile, Serie Recursos Minerales y Energéticos (n.27), 72 p., Santiago.
Wilson, J., Grocott, J., 1999. The emplacement of the granitic Las Tazas complex, northern Chile: the relationship between local and regional strain. J. Struct. Geol. 21 (11), 1513–1523. https://doi.org/10.1016/S0191-8141(99)00117-0.
Wiltschko, D.V., Morse, A., 2001. Crystallization pressure versus "crack seal" as the mechanism for banded veins. Geology 29, 79–82.
Woodcock, N., Dickson, J., Tarasewicz, J., 2007. Transient permeability and reseal hardening in fault zones: evidence from dilation breccia textures. Geological Society, London, Special Publications, vol. 270, pp.43–53.
Young, A., Flament, N., Maloney, K., Williams, S., Matthews, K., Zahirovic, S., Müller, R.D., 2018. Global kinematics of tectonic plates and subduction zones since the late Paleozoic Era. Geosci. Front. https://doi.org/10.1016/j.gsf.2018.05.011.